Acta Biomaterialia 200 (2025) 591–609

Contents lists available at ScienceDirect

Acta Biomaterialia

journal homepage: www.elsevier.com/locate/actbio

Full length article

Dextran guanidinylated carbon dots with antibacterial and immunomodulatory activities as eye drops for the topical treatment of MRSA-induced infectious keratitis

Menghan Zhang [a,1], Yiyang Wang [b,c,1], Chenfang Miao [a,1], Shuwei Lin [d], Ying Zheng [a], Xiaoyan Lin [a], Yao Wang [a], Xinhua Lin [a], Xiaofeng Zhu [b,c], Shaohuang Weng [a,*]

[a] Department of Pharmaceutical Analysis, School of Pharmacy, Fujian Medical University, Fuzhou 350122, China
[b] Department of Oral Maxillo-Facial Surgery, the First Affiliated Hospital, Fujian Medical University, Fuzhou, 350005, China
[c] Fujian Key Laboratory of Oral Diseases & Fujian Provincial Engineering Research Center of Oral Biomaterial & Stomatological Key Lab of Fujian College and University, School and Hospital of Stomatology, Fujian Medical University, Fuzhou, 350004, China
[d] School of Basic Medical Sciences, Fujian Medical University, Fuzhou 350122, China

ARTICLE INFO

Keywords:
Carbon dots
Bacterial biofilm
Antibacterial molecular mechanism
Immunomodulation
Bacterial keratitis

ABSTRACT

Bacterial keratitis (BK) develops rapidly and can cause serious consequences, requiring timely and efficient treatment. As the main treatment strategy, antibiotic eye drops are still plagued by bacterial resistance by biofilms and failure to modulate immunity. Herein, dextran guanidinylated carbon dots (DG-CDs) with antimicrobial and immunomodulatory properties were developed. DG-CDs with the graphitized core-like structure with the ordered arrangement of carbon atoms and surface groups of C—N, C—O—C, and -OH were thoroughly characterized and modeled as a graphene-like sheet. DG-CDs exhibited strong antimicrobial and anti-biofilm activities with a minimum inhibitory concentration (MIC) of 5 μg/mL against methicillin-resistant *Staphylococcus aureus* (MRSA). Molecular docking based on well-characterized structures of DG-CDs revealed that DG-CDs had strong affinity for key bacterial proteins including FtsA, IcaA and ArgA, which were confirmed by corresponding RT-qPCR and transcriptomics. Furthermore, DG-CDs regulated macrophage polarization by inhibiting the M1 subtype and promoting the transition to the M2 subtype. *In vivo* experiments illustrated that DG-CDs used as eye drops significantly attenuated corneal infection, enhanced the expression of anti-inflammatory factors, and effectively promoted corneal repair in MRSA-infected BK. Overall, this study provides a promising antibacterial nanomaterial with clarified properties and acting mechanism for treating BK as eye drops.

Statement of significance: Besides bacterial invasion, bacterial keratitis (BK) also suffers from immune imbalance, which further impairs corneal healing. Current antibiotic eye drops are plagued by bacterial resistance and their inability to modulate immunity. Herein, dextran guanidinylated carbon dots (DG-CDs) with dual functions of antimicrobial and immunomodulatory were developed for treating MRSA infected BK. DG-CDs, with clarified structure and surface groups, exhibited strong antimicrobial activity and no detectable resistance. Molecular docking, based on well-characterized structures of DG-CDs, was achieved to reveal the antibacterial mechanism, which was subsequently confirmed by RT-qPCR and transcriptomics. In addition, DG-CDs exhibited an effective healing ability in an MRSA-infected rat keratitis model by exerting antibacterial activity and regulating macrophage polarization from M1 type to M2 type. DG-CDs represent a promising antibacterial nanomedicine with clarified properties and acting mechanism for treating bacterial infection.

1. Introduction

As the outermost part of the eye, the cornea is susceptible to inflammation caused by microorganisms, trauma, and external irritants [1–3]. Bacterial keratitis (BK) is a serious infectious condition of the cornea with early symptoms including increased tearing, eye pain,

---

* Corresponding author.
E-mail address: shweng@fjmu.edu.cn (S. Weng).
[1] Contributed equally to this work.

https://doi.org/10.1016/j.actbio.2025.05.032
Received 16 January 2025; Received in revised form 15 April 2025; Accepted 11 May 2025

decreased vision and photophobia [4]. Untimely controlled BK can quickly progress corneal perforation and intraocular infection, and in severe cases, can result in ocular atrophy or even blindness [5–7]. In addition, bacteria activate the local immune response in the infectious cornea [8–10]. Typically, immune cells, particularly macrophages, rapidly accumulate at the site of infection and release various cytokines and inflammatory mediators to eliminate the invading pathogens [11, 12]. Under normal circumstances, the immune system regulates the intensity and duration of the inflammatory response to facilitate tissue repair [13]. However, in infectious conditions or when there is an imbalance in immune regulation, inflammation can persist at the site of keratitis hindering tissue repair and causing further damage [14]. Therefore, in addition to the use of antimicrobials to control infection, immunomodulation is necessary to reduce the inflammatory response for repairing keratitis [15,16].

For BK, topical eye drops are a first-line and effective treatment due to their high localized concentration and efficacy at the infection site [17]. However, the rise of antibiotic resistance has diminished the effectiveness of traditional antibiotic eye drops, contributing to the emergence of multidrug-resistant pathogens associated with keratitis, such as methicillin-resistant *Staphylococcus aureus* (MRSA). These pathogens can form biofilms, evading both the host immune system and the antimicrobial effect of drugs, leading to persistent infections [18, 19]. To combat antibiotic resistance, membrane-active antimicrobials present a promising therapeutic strategy, as conventional antibiotics often fail due to their limited biofilm penetration [20] and high susceptibility to resistance development [21]. Additionally, when MRSA invades the cornea, it infects both the epithelial and stromal layers, causing pathological changes such as corneal opacity, edema, and loss of iris texture and pupil definition. The infection also triggers an inflammatory cascade, recruiting large numbers of immune cells to the site [22]. Although the release of pro-inflammatory cytokines helps control the infection stimulated by MRSA, an excessive immune response can exacerbate corneal damage [23,24]. Consequently, modulating the immune response—particularly by upregulating anti-inflammatory cytokines like IL-10 and IL-4—is one of the key strategies for treating keratitis [25]. Anti-inflammatory factors such as IL-10 not only effectively balance the immune response and reduce corneal damage caused by excessive inflammation, but also promote the regeneration and repair of corneal epithelial cells to facilitate healing [26–28]. Therefore, the development of eye drops with both antibacterial and immunomodulatory functions is critical for the control and treatment of BK, as they can act quickly and effectively on the infected area of the eye to directly inhibit and even eliminate bacteria, while modulating the immune response to reduce inflammation for regeneration of the damaged cornea.

Non-antibiotic strategies for the development of antimicrobial drugs include the exploration of natural antimicrobial products, antimicrobial peptides, vaccines, bacteriophages, and nanomedicines [29,30]. Among these, nanomedicine holds particular promise for addressing bacterial resistance due to its versatile mechanisms of action [30–32]. Specific nanomaterials, such as metal and metal oxide nanoparticles [33–35], carbon-based nanomaterials [36], polymer-based nanomaterials [37], nanozymes [38], and light-sensitive nanomaterials [39,40], can combat bacteria through multiple pathways, including reactive oxygen species (ROS) generation [41], membrane disruption [42], photodynamic and photocatalytic effects [43,44], gene disruption [45] and electron transport inhibition [46]. Studies suggest that well-designed synthesis strategies and surface modifications can yield nanomaterials with potent antimicrobial activity, as exemplified by current nanotherapeutic for keratitis in Table S1. However, few nanomedicines have demonstrated dual functionality, combining antibacterial effect with immunomodulation to enhance healing.

Carbon dots (CDs), zero-dimensional carbon nanomaterials with a uniform sub-10 nm size [47], are particularly promising due to their high surface area, which enables extensive interactions with biological and chemical molecules [48]. By optimizing precursor selection [49], refining synthetic and purification methods [50,51], and modifying surface functional groups [52,53] or charge properties [54], CDs have emerged as promising alternatives to traditional antibiotics for antimicrobial applications [55]. Their antibacterial mechanisms include ROS production, membrane disruption, DNA damage, and metabolic interference [56,57]. Nevertheless, research on antibacterial CDs faces some challenges. The precise interaction between CDs and specific bacterial membranes or proteins remains poorly understood, largely due to the lack of knowledge regarding the specific structures of CDs [58]. The diverse ranges of sources and synthesis methods of prepared CDs give rise to a multitude of surface functional groups and physicochemical properties, which in turn render the interaction between CDs and bacteria a highly intricate and challenging phenomenon for precise analysis [59]. Thus, a deeper molecular-level investigation is needed to explore the antimicrobial mechanisms of CDs more comprehensively. Encouragingly, recent studies demonstrate that CDs with different but controlled functionalities can be engineered by adjusting feedstocks or synthesis conditions [60]. For example, selectively tuning the hydrothermal synthesis approaches and raw materials can yield CDs with specific fluorescence responses to hydroxyl radicals [61,62]. The feasibility of creating CDs with different functionalities suggests that the design and preparation of CDs with appropriate source materials and methods will enable the development of biocompatible CDs with dual antimicrobial and immunomodulatory properties—an underexplored yet highly promising avenue for therapeutic applications.

Dextran (DEX) is a natural polysaccharide with biocompatibility and potential immune-regulating properties, and its structural features can target extracellular polymeric substances (EPS) of bacteria to enhance adsorption and permeation [63–65]. Polyhexamethylene guanidine (PHMG) exhibits certain antibacterial activity through guanidine groups but has cytotoxicity. Citric acid (CA), an eco-friendly carbon source, can form a stable carbon core structure when combined with other precursors for preparing CDs. In general, the synthesized CDs is expected to preserve the functional groups of the raw materials. Accordingly, DEX, PHMG, and CA were chosen as raw materials for the design of functional carbon dots in this work. As shown in Fig. 1, dextran guanidinylated carbon dots (DG-CDs) were controllably prepared using a rapid, controlled hydrothermal method. The synthesized DG-CDs exhibited ultra-small size, positive zeta potential, and surface functional groups ($C{=}N$/$C{-}N$, $C{-}O{-}C$, -OH), enabling strong bacterial adsorption, broad-spectrum antibacterial activity, low drug resistance risk, and good biocompatibility. *In vitro* experiments showed that DG-CDs effectively inhibited and removed biofilms of *S. aureus* and MRSA. Molecular docking, RT-qPCR and transcriptomic analyses preliminarily clarified the molecular mechanisms underlying the antibacterial effects of DG-CDs. Flow cytometry analysis demonstrated that DG-CDs promoted the conversion of inflammatory (M1) macrophages to anti-inflammatory (M2) macrophages, reducing the inflammatory response. *In vivo*, DG-CDs administered as eye drops showed significant efficacy in treating MRSA-induced keratitis, owing to their combined antibacterial and immunomodulatory activities that promoted corneal repair, highlighting their potential in topical therapeutic applications. These results offer valuable conceptual framework for the development bioactive CDs with well-defined therapeutic efficacy, structure, and mechanisms of action.

2. Materials and experiment methods

2.1. Materials

Citric acid, phenol, acetic acid, vancomycin hydrochloride, methanol, and ethanol were purchased from Shanghai Aladdin Biochemical Technology Co., Ltd. PHMG was purchased from Shanghai Macklin Biochemical Technology Co., Ltd. Dextran (Dex, MW 20,000) was provided by Beijing Wokai Biotechnology Co., Ltd. Sodium chloride,

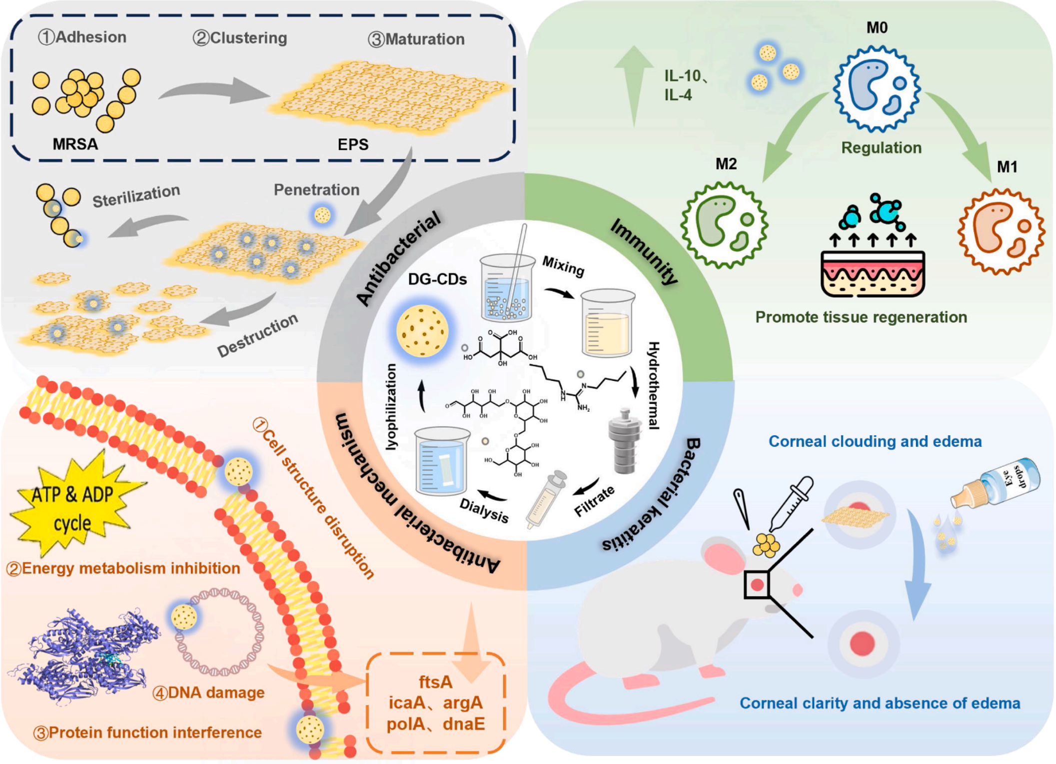

Fig. 1. Synthesis procedure, properties, mechanism and local application of DG-CDs.

sodium bicarbonate, dextrose, dibasic sodium phosphate, potassium chloride, magnesium chloride, and calcium chloride were provided by China National Pharmaceutical Group. Sodium hyaluronate eye drops were provided by Chengdu Pusch Pharmaceutical Co., Ltd. Glutaraldehyde fixative (2.5 %, for electron microscopy) was purchased from Nanjing Sembega Biotechnology Co., Ltd. Fetal bovine serum (FBS), live/dead BacLight Bacterial Viability Kit (L7012), and minimum essential medium (MEM) were purchased from Invitrogen Gibco (USA). Lysozyme, rabbit serum and 0.1 % crystal violet staining solution were purchased from Beijing Solepol Technology Co., Ltd. Trypsin, proteinase K, and recombinant proteinase K were purchased from Sangon Bioengineering (Shanghai) Co., Ltd. BCA kit and adenosine triphosphate (ATP) assay kit were purchased from Shanghai Biyuntian Biotechnology Co., Ltd. Tryptic soy peptone liquid medium (TSB), Mueller-Hinton (MH) broth, and Mueller-Hinton agar were purchased from Qingdao Haibo Biotechnology Co., Ltd and autoclaved at 121 °C for 20 min before use.

2.2. *Cell culture and bacterial solution configuration*

Human renal cortical proximal tubule epithelial cells (HK-2) and human lens epithelial cells (HLE-B3) were purchased from Wuhan Posay Life Sciences Co., Ltd. and cultured in MEM supplemented with 10 % FBS at 37 °C in a 5 % CO_2 incubator. *S. aureus* (ATCC6538) and MRSA (ATCC43300) were purchased from Shanghai Luwei Science and Technology Co., Ltd. Single colonies were streaked on agar plates and incubated at 37 °C. Colonies were then inoculated into saline, adjusted to 0.5 McFarland turbidity, yielding a bacterial suspension of 1.5×10^8 CFU/mL.

2.3. *Synthesis of DG-CDs*

The 0.4 g CA, 0.4 g DEX, and 50 mg PHMG were dissolved in 20 mL ultrapure water. The solution was transferred to a 50 mL PTFE hydrothermal reactor and heated at 150 °C for 6 h. After cooling, the solution was filtered through a 0.22 μm PES membrane. The filtrate was dialyzed using a dialysis membrane with a molecular weight cutoff of 500–1000 Da for 48 h, and subsequently freeze-dried to obtain solid DG-CDs.

2.4. *Characterization of DG-CDs*

The particle size and morphology of the DG-CDs were characterized using a transmission electron microscope (TEM, JEM-2100F). The water contact angle of the DG-CDs was determined using an optical contact angle meter (Attension Theta Lite). The zeta potential was analyzed using a Zetasizer Nano ZS90 instrument. UV–vis absorption spectra were obtained using a UV-2450 spectrophotometer and the fluorescence properties of the DG-CDs were analyzed using a Cary Eclipse fluorescence spectrophotometer. Characterization of the carbon structure was carried out using a Bruker D8 advance X-ray diffractometer. The structure and defect states of the DG-CDs were determined using a LabRam HR Evolution Raman spectrometer. The Fourier transform infrared (FTIR) spectra of the DG-CDs were recorded using a Nicolet iS50 infrared spectrometer. The ^1H and ^{13}C NMR spectra of the DG-CDs in D_2O were recorded using an AVANCE III HD instrument. The X-ray photoelectron spectroscopy (XPS) measurements were performed using a Theta probe spectrometer (Thermo Fisher Scientific).

2.5. *Determination of minimum inhibitory concentration (MIC)*

The antimicrobial activity of DG-CDs was assessed using the broth dilution method to determine the MIC against common pathogens, including *Staphylococcus aureus* (*S. aureus*, ATCC6538), Methicillin-resistant *Staphylococcus aureus* (MRSA, ATCC43300), *Staphylococcus epidermidis* (*S. epidermidis*, ATCC12228), *Listeria monocytogenes* (*L. monocytogenes*, ATCC19115), *Enterococcus faecalis* (*E. faecalis*, ATCC29212), *Escherichia coli* (*E. coli*, ATCC25922), *Klebsiella pneumoniae* (*K. pneumoniae*, ATCC10031), *Pseudomonas aeruginosa* (*P. aeruginosa*, ATCC9027), *Salmonella paratyphi B* (*S. paratyphi B*, CMCC (B)50094), and *Serratia marcescens* (*S. marcescens*, CMCC(B)41002). Colonies cultured on agar plates for 18–24 h were picked and used to prepare a bacterial suspension with 0.5 McFarland turbidity, yielding a concentration of 1.5×10^6 CFU/mL by 1:100 dilution with MH broth. Thirteen sterile test tubes were labeled and filled with 1 mL of MH broth each. DG-CDs (1280 μg/mL) were added to tube 1 and mixed, then serially diluted to tube 11. The negative control (2 mL MH medium) and positive control (1 mL MH medium and 1 mL bacterial suspension) were set up. The final DG-CDs concentrations ranged from 320 to 0.3125 μg/mL. 1 mL of bacterial suspension was added to each tube, and incubated for 24 h. The MIC was determined by visual inspection, as the lowest concentration showing no visible bacterial growth.

2.6. Determination of the bacteriostatic curve

Different concentrations of DG-CDs (50 μL) were added to 96-well plates (NEST, Wuxi, China), followed by 50 μL of bacterial suspension (1.5×10^6 CFU/mL). The plates were mixed and incubated at 37 °C for 48 h. OD_{600} values were recorded every 2 h during the first 24 h and every 12 h thereafter until the 48-hour incubation ended.

2.7. Bacterial plate coating assay

Following the method in Section 2.6, DG-CDs at various concentrations were prepared and incubated with the bacterial solution. A pipette was used to transfer a specific volume of the bacterial solution, which was evenly spread onto labeled agar plates using a sterile spreader. The plates were incubated inverted in a constant-temperature incubator under appropriate temperature and humidity conditions. After 24 h, the morphology, number and distribution of colonies were observed and recorded.

2.8. Antimicrobial stability testing

To evaluate the long-term antimicrobial stability of DG-CDs, the MIC against *S. aureus* and MRSA was determined after storing the aqueous solution of DG-CDs at 4 °C for 1, 7, 14, 30, 60, 90, 120, 180, 240 and 360 days using the broth dilution method. Additionally, the MIC was tested after subjecting the DG-CDs solution to 2 h of continuous 365 nm UV irradiation and to water bath treatments at temperatures ranging from 20 °C to 90 °C for 2 h. The stability of DG-CDs in protease and serum was assessed by measuring their antibacterial activity in MH broth containing trypsin, proteinase K, 50 % FBS, and 50 % rabbit serum. To assess the antibacterial stability of the prepared DG-CDs in artificial tear fluid, artificial tear fluid was first prepared with the following components: sodium chloride (7.14 mg/mL), sodium bicarbonate (2.10 mg/mL), dextrose (0.92 mg/mL), lysozyme (1.70 mg/mL), dibasic sodium phosphate (0.42 mg/mL), potassium chloride (0.38 mg/mL), magnesium chloride (0.20 mg/mL), and calcium chloride (0.15 mg/mL). Subsequently, the DG-CDs powder was dissolved in the artificial tear fluid, and the MIC against *S. aureus* and MRSA was measured on days 1, 3, 5, 7, 14, 21, and 28. In addition, to simulate actual ophthalmic application conditions, a commercially available sodium hyaluronate-based eye drop solution was used as the base formulation. The DG-CDs powder was dissolved in this eye drop solution. The MICs of DG-CDs in the eye drop solution against *S. aureus* and MRSA were similarly measured on days 1, 3, 5, 7, 14, 21, and 28.

2.9. Assessment of drug resistance development

Bacterial resistance to DG-CDs was evaluated using the broth dilution method. The initial MICs of DG-CDs against *S. aureus* and MRSA were determined as described above. The bacterial suspension from sub-MIC tubes was spread onto agar plates and incubated at 37 °C for 24 h. Colonies were picked, suspended in 1.5×10^8 CFU/mL, and used for the subsequent MIC assay. This procedure was repeated daily, and MIC values were recorded until the 30th day. The final MIC value was compared with the initial MIC to assess the development of drug resistance. A similar set of experiments was conducted with vancomycin to evaluate the potential resistance of *S. aureus* and MRSA.

2.10. Bacterial biofilm inhibition and disruption assay

Each well of a 96-well plate was inoculated with 50 μL of *S. aureus* and MRSA suspension (1.5×10^8 CFU/mL) cultured in TSB medium, followed by 50 μL of different concentrations of DG-CDs (0 to 160 μg/mL). The plates were incubated at 37 °C for 2 days to assess bacterial biofilm formation. After incubation, the plate was washed three times with PBS to remove non-adherent bacteria, then fixed with 100 μL methanol for 10 min. After fixation, the plates were washed, air-dried, stained with 0.1 % crystal violet, and rinsed until the negative control wells were colorless. Crystal violet was dissolved with 33 % acetic acid, and the OD_{570} value was measured. The inhibition rate was calculated using the formula:

$$\text{Inhibitionrate}(\%) = (OD_a - OD_b)/OD_a \times 100\%$$

For biofilm disruption, 100 μL of *S. aureus* and MRSA suspension (1.5×10^8 CFU/mL) was inoculated into 96-well plates and incubated for 24 h. DG-CDs were then added (0 to 160 μg/mL), and the procedure followed the same steps as for inhibition. The elimination rate was calculated using the formula:

$$\text{Eliminationrate}(\%) = (OD_a - OD_b)/OD_a \times 100\%$$

Where OD_a and OD_b represent the optical densities with and without DG-CDs intervention.

2.11. Bacterial live-dead staining

To assess the biofilm destruction by DG-CDs, live/dead staining was performed using SYTO 9 (6 μmol/L) and PI (30 μmol/L), and biofilm changes in *S. aureus* and MRSA were visualized using CLSM. *S. aureus* and MRSA suspensions were added to confocal Petri dishes and incubated for 48 h to form biofilms. After biofilm formation, the dishes were washed twice with PBS, and DG-CDs were added for 24 h of co-incubation. The biofilms were stained in the dark at 37 °C for 30 min, then washed three times with PBS. CLSM images were captured and analyzed using LAS X software (Leica, Germany).

2.12. Scanning electron microscopy (SEM) of the bacterial morphological differences

SEM was used to observe bacterial morphology before and after DG-CDs' treatment. Bacterial suspension ($OD_{600} = 0.5$–0.8) was mixed with equal volumes of DG-CDs and MH broth for 6 h. After centrifugation, the precipitate was washed with PBS, fixed with 2.5 % glutaraldehyde for 30 min at room temperature, then stored at 4 °C overnight. The bacteria were dehydrated in a gradient ethanol series (10 min per step), freeze-dried for 2.5 h, and coated with gold for observation.

2.13. Effect of DG-CDs on zeta potentials of bacteria

DG-CDs were added to *S. aureus* or MRSA suspensions and incubated at 37 °C for 6 h to allow full interaction. The same volume of MH broth without DG-CDs was served as a control. After incubation, both groups were centrifuged, and the bacterial precipitates were washed 2–3 times with PBS to remove free DG-CDs. The zeta potential of the washed bacteria was measured in PBS.

2.14. Effect of DG-CDs on bacterial ATP

1 mL of *S. aureus* or MRSA (1 × 10^8 CFU/mL) was incubated with different concentrations of DG-CDs for 6 h at 37 °C. After centrifugation, the supernatant was discarded, and the bacteria were resuspended. Then, 200 μL of lysate was added and incubated at 4 °C. The supernatant was centrifuged at 12,000 g for 5 min at 4 °C, and ATP was measured using an ATP kit.

2.15. Determination of polysaccharide and protein content of EPS

EPS substrates were obtained by culturing *S. aureus* and MRSA biofilms. 800 μL of bacterial suspension (1.5 × 10^8 CFU/mL in TSB medium) was added to a 48-well plate and incubated at 37 °C for 24 h. DG-CDs at different concentrations were then added and incubated for an additional 24 h. The medium was discarded, and the plate was washed three times with saline to collect EPS. The EPS samples were vortexed and sonicated for 5 min.

EPS polysaccharide content was determined using a modified sulfuric acid-phenol method. 200 μL of EPS sample was mixed with 600 μL of 98 % sulfuric acid and 200 μL of phenol, incubated at 50 °C for 30 min, and OD_{490} was measured.

Protein content in EPS was measured using the BCA protein assay kit. 20 μL of EPS samples were added and mixed with 200 μL of BCA working reagent in the well of 96-well plates. The solution was allowed to stand at 37 °C for 30 min for measuring OD_{562}.

2.16. Monitoring the interaction of DG-CDs and ssDNA

100 μL of different concentrations of DG-CDs were mixed with 100 μL of PBS containing 100 nM Fluorescein Amidite-DNA (FAM-DNA) and incubated at room temperature in the dark for 10 min. Then, the fluorescence emission spectra were measured with excitation at 488 nm. The fluorescence quenching rate of FAM was calculated using the equation of $(F_0\text{-}F)/F_0$, F and F_0 represent the fluorescence intensities of F-DNA at 520 nm in the presence/absence of DG-CDs, respectively.

2.17. Molecular docking studies

Protein structures were downloaded from the Protein Data Bank (PDB format), AutoDock vina 1.2.5 was used for molecular docking with ligand molecules and molecular interactions were visualized using the Pymol visualisation tool.

2.18. Real-time quantitative reverse transcription PCR (RT-qPCR) to detect the expression of virulence genes

RT-qPCR was used to detect the expression of virulence genes (ftsA, icaA, agrA, polA, dnaE, rpoB, rpoA) in *S. aureus* and MRSA. Bacteria were cultured in TSB medium with or without DG-CDs for 48 h. After centrifugation, the medium was removed, and the bacteria were washed with PBS. Lysozyme (1 mg/mL) was added, and the mixture was incubated at 37 °C for 15 min, followed by centrifugation to collect total RNA using the Trizol method. RNA was reverse transcribed to cDNA, and RT-qPCR was performed using an AB2720 PCR instrument (Applied Biosystems, USA) with a fluorescence quantification kit (Transgen). The reaction mixture included 0.2 μL of each primer, 5 μL of 2×PerfectStart Green qPCR SuperMix, and 5.6 μL of cDNA. PCR conditions were: 94 °C for 30 s (activation), 94 °C for 5 s (denaturation), 60 °C for 30 s (annealing), cycling 40–45 times, and fluorescence data recording. Results were analyzed by the $2^{-\Delta\Delta CT}$ method, with rpoA as the internal reference gene (Table 1).

Table 1
The primer sequence of the PCR of this work.

Name Sequence (50–30)	Sequence (5′–3′)
icaA	F:CAGTCAATACTATTTCGGGTGTCT R:GCAAGCGGTTCATACTTAATACG
agrA	F:CCTCGCAACTGATAATCCTTATGA R:TGCTTACGAATTTCACTGCCTAA
ftsA	F:TGAAGCATGTGGTGTTGATGTATT R:TAATATCACGCCCTGCCATTTC
polA	F:GGCGTCCACCTTTATATTCACTAT R:ACAAAGCAGGCATTCATACCA
dnaE	F:TCGTTCGGCTTCAGTCATTG R:CTACACATGCGGCAGGAATT
rpoB	F:TCGGTGAGATGGAGGTATGG R:TCGGAATGATTCTGGAACACTTG
rpoA	F:CTGCTAATGCGTAACCTCTACC R:CGTGATGAAGGCGAAGTAACA

2.19. Transcriptomic analysis

MRSA was cultured in TSB medium at 37 °C for 24 h. Subsequently, a bacterial suspension (10^8 CFU/mL) was added to TSB medium containing 80 μg/mL DG-CDs and incubated at 37 °C for an additional 4 h. Transcriptomic analysis, including total RNA extraction and subsequent bioinformatics data processing, was performed by WANCHENG Biomedical Technology Co., Ltd. (Shanghai, China).

2.20. Flow cytometry to detect the pro-immunological properties of DG-CDs

LPS stimulation was applied to simulate inflammatory conditions. RAW264.7 cells were incubated for 24 h with either different concentrations of DG-CDs alone or in combination with 1000 ng/mL LPS. After incubation, cells were collected with a scraper, centrifuged, and washed with PBS. Cells were then fixed with 4 % paraformaldehyde for 30 min, followed by washing and membrane permeabilization with 0.1 % Triton-X100 for 10 min. Antibodies against CD86 and CD206 were added, and cells were incubated in the dark for 30 min. After washing, fluorescence intensity was analyzed using a flow cytometer.

2.21. ELISA for macrophage induction by DG-CDs

According to the experimental method described in Section 2.20, RAW 264.7 cells were treated as described. Following incubation, the cell culture supernatants were collected, and the levels of IL-4 and IL-10 were determined using ELISA kits.

2.22. Cytotoxicity

A cell viability assay (CCK-8) was used to assess the cytotoxicity of DG-CDs on HK-2 and HLE-B3 cells. A total of 100 μL of cell suspension (7 × 10^3 cells/well) was added to each well of a 96-well plate. For the blank group, an equal volume of medium was added instead. Cells were incubated at 37 °C with 5 % CO_2 for 24 h. Then, cells were exposed to various concentrations of DG-CDs for another 24 h. 10 μL of CCK-8 solution was added to each well and incubated for 1 h. Absorbance at 450 nm was measured using a microplate reader, and cell viability was calculated accordingly:

$$\text{Cellviability}(\%) = \left(\text{OD}_{\text{experiment}} - \text{OD}_{\text{blank}}\right) / \left(\text{OD}_{\text{control}} - \text{OD}_{\text{blank}}\right) \times 100\%$$

Where the experimental group is DG-CDs treated cell samples. The control group is untreated cell samples, while the blank group contained only culture medium without cells.

2.23. Hemolysis test

The blood samples were obtained from the First Affiliated Hospital of Fujian Medical University based on the ethics committee approval ([2015]084-1). A hemolysis test for DG-CDs was conducted using red blood cells (RBCs). The experimental conditions were based on the blood compatibility assessment framework of ISO 10993-4:2017, with incubation for 3 h under static conditions as recommended by ASTM F756-17. Erythrocytes were suspended in saline to form a slurry. RBC suspensions were incubated with various concentrations of DG-CDs at 37 °C for 3 h. Distilled water and saline were used as positive and negative controls, respectively. After incubation, the samples were centrifuged, and the absorbance of the supernatant at 540 nm was measured. The hemolysis rate was calculated based on the absorbance

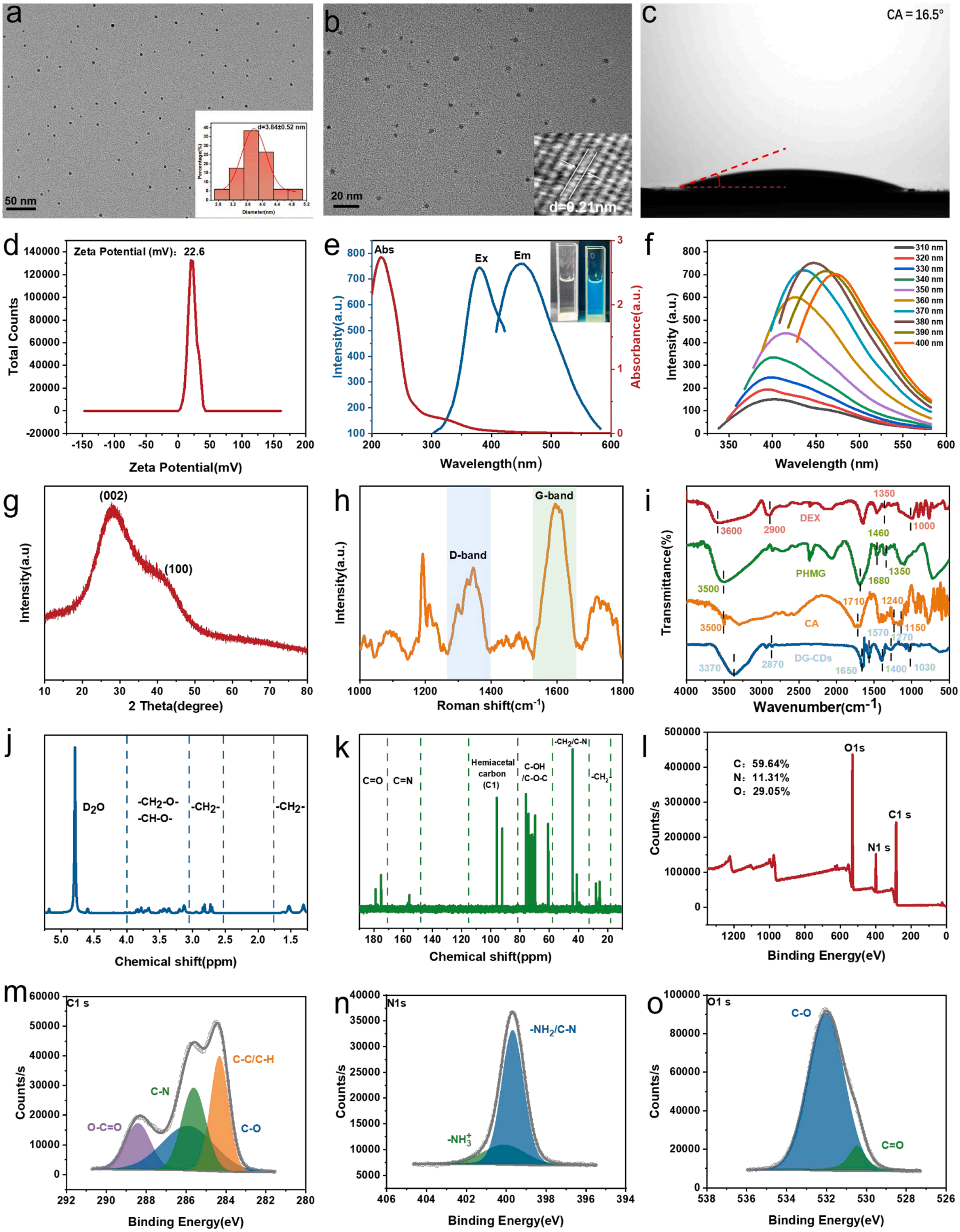

Fig. 2. Preparation and characterization of DG-CDs. (a, b) TEM images with different magnification, and the insets are the statistical graph of particle size distribution and HRTEM, respectively. (c) Water contact angle. (d) Zeta potential map. (e) UV–vis absorbance and fluorescence spectra, and images of aqueous solution under sunlight and UV excitation. (f) Fluorescence spectra of DG-CDs at different exciting wavelengths. (g) XRD diagram. (h) Raman diagram. (i) FTIR spectra of CA, DEX, PHMG and DG-CDs. (j) ^{13}C NMR spectrum. (k) ^{1}H NMR spectrum. (l) Full XPS spectrum; (m-o) high resolution XPS spectra of C 1 s (m) N 1 s (n) and O 1 s (o).

difference:

$$\text{Hemolysisrate}(\%) = \left(\text{OD}_{\text{sample}} - \text{OD}_{\text{negative}}/\text{OD}_{\text{positive}} - \text{OD}_{\text{negative}}\right) \times 100\%$$

2.24. Intervention in a rat model of keratoconus

This study was approved by the Institutional Animal Care and Use Committee of Fujian Medical University (IACUC FJMU 2024-0250). The *in vivo* efficacy of DG-CDs against MRSA infection was tested using a rat corneal model. Following anesthesia, the rat corneas were scratched using a 25-gauge needle, and 20 μL of MRSA suspension (1 × 10^9 CFU/mL) was applied to induce keratitis. The infected corneas were examined after 24 h using slit-lamp microscopy. Sprague-Dawley rats (300 g) were randomly divided into three groups ($n = 6$ per group): the blank control group received saline eye drops, the positive control group received 40 μL of vancomycin (16 μg/mL), and the experimental group received 40 μL of DG-CDs drops. Treatments were administered every 24 h.

Before treatment, bacteria were collected from the cornea using a cotton swab to assess changes in bacterial colonization. Slit lamp examinations (SLE) evaluated corneal morphology, scoring parameters included conjunctival congestion, oedema, iritis, and interstitial infiltration. At the end of the experiment, rats were euthanized, and their corneas were harvested for hematoxylin and eosin (H&E) staining and immunohistochemical analysis of IL-4 and IL-10 to evaluate therapeutic effects. Additionally, heart, liver, spleen, lung, and kidney tissues were collected for HE staining to assess potential systemic toxicity.

2.25. Statistical analysis

Data were presented as mean ± standard deviation and analyzed using one-way ANOVA followed by a *t*-test. Statistical significance was defined as follows: $^{*}P < 0.05$, $^{**}P < 0.01$, $^{***}P < 0.001$, $^{****}P < 0.0001$; $P \geq 0.05$ was considered not significant (ns). All graphs and statistical analyses were performed using GraphPad Prism (version 9) and OriginPro (2021). For histological evaluation, at least three fields per tissue section were analyzed, followed by quantitative image analysis using ImageJ software.

3. Results and discussion

3.1. Characterization of DG-CDs

First, the morphology and size distribution of DG-CDs were characterized by TEM. DG-CDs were monodispersed and quasi-spherical nanoparticles with uniform size, with an average diameter of 3.84 nm (Fig. 2a and b). High-resolution TEM (HRTEM) analysis (inset of Fig. 2b) confirmed the crystalline structure of DG-CDs, displaying distinct lattice fringes with a spacing of 0.21 nm, corresponding to the (100) crystallographic plane of graphitic carbon [66]. The hydrophilicity and surface charge of DG-CDs were also investigated. As shown in Fig. 2c, the water contact angle value of DG-CDs was tested to be 16.5°, indicating hydrophilicity. The zeta potential of +22.6 mV indicated the positive charge of DG-CDs (Fig. 2d). Appropriate hydrophilicity is a key determinant in optimizing material properties to maximize biocompatibility without compromising antimicrobial efficacy [67]. UV–vis absorbance spectrum of DG-CDs (Fig. 2e) showed the absorption peak at 217 nm, corresponding to the π-π* transition of C═C, and the shoulder peak between 340 nm and 400 nm, attributed to the *n*-π* transition of C═O and C═N. Fluorescence spectra demonstrated maximum emission at 450 nm under the optimal excitation of 380 nm. DG-CDs in water appeared as a pale-yellow solution under natural light and showed blue fluorescence under UV light. In addition, Fig. 2f shows that the emission peaks of DG-CDs gradually red-shifted with increased excitation wavelengths from 310 nm to 400 nm, suggesting the excitation wavelength-dependent fluorescence behavior.

The carbonized structure and defect characteristics of DG-CDs were studied. The XRD pattern (Fig. 2g) revealed a distinct diffraction peak at approximately 27°, corresponding to the (002) crystallographic plane of the graphite-like structure, indicating the presence of relatively ordered graphitized core in DG-CDs [68]. Compared to the standard ordered graphitic structure with 2θ = 26.5° (d002 = 0.34 nm), the slight shift to a higher angle can be attributed to a small amount of disordered carbon (sp3) formed during the carbonization process [69]. In addition, the broad peak near 42° is the d-spacing of 0.21 nm at the graphite (100) plane [70], consistent with the HRTEM results that demonstrate the crystallinity of DG-CDs. The Raman spectrum (Fig. 2h) showed characteristic peaks at 1345 cm^{-1} (D band) and 1596 cm^{-1}(G band). The D band corresponds to disordered carbon, indicating heteroatom doping and surface defects in the graphene structure, while the G band represents graphitized carbon, reflecting in-plane vibration of sp^2 hybridized carbon atoms. The intensity ratio ($I_D/I_G = 0.55$) suggests DG-CDs possess high graphitization with moderate defects density, consistent with XRD results [71]. In addition, Raman mapping also showed that DG-CDs had higher peaks at 1090 cm^{-1}, 1191 cm^{-1} and 1729 cm^{-1}. Together with the reaction precursors, the peak at 1090 cm^{-1} was mainly related to the stretching vibration of the C—O—C bond from DEX, the peak at 1191 cm^{-1} may be related to the vibration of the C—N bond or the C—O bond from the guanidine group in PHMG and the carboxylate group in CA. The band at 1729 cm^{-1} was the C═O stretching vibration from the carboxyl group in CA, suggesting the presence of group residues in DG-CDs. The observed background noise and baseline drift were likely due to the abundance of surface functional groups on DG-CDs [72].

The structure and chemical composition of DG-CDs were further investigated. As shown in Fig. 2i, the FTIR spectrum of CA exhibited the characteristic peaks, including a C═O stretching vibration at 1710 cm^{-1}, a C—O stretching vibration at 1240 cm^{-1}, and a C—O bending vibration at 1150 cm^{-1}. In addition, the FTIR spectrum of PHMG displayed an N—H stretching vibration absorption around 3500 cm^{-1}, a C═O stretching vibration peak at 1680 cm^{-1}, and the C—H bending vibration absorption peak near 1460 cm^{-1} and C—N stretching vibration absorption peak at 1350 cm^{-1}. The FTIR spectrum of DEX exhibited the broad absorption peak of O—H stretching vibration in the range of 3200–3600 cm^{-1}, a C—H stretching vibration absorption peak at 2900 cm^{-1}, a C—C bending vibration absorption peak near 1350 cm^{-1}, and a C—O stretching vibration of ether bond in polysaccharides at 1000 cm^{-1}. The absorption peak of DG-CDs at 3370 cm^{-1} was the typical O—H or N—H stretching vibration. The C—H stretching vibration and bending vibration were observed at 2870 cm^{-1} and 1400 cm^{-1}, respectively. The peaks at 1650 cm^{-1} and 1570 cm^{-1} were attributed to C═N stretching and C═O stretching, respectively. The peaks at 1270 cm^{-1} and 1050 cm^{-1} were ascribed to C—N and C—O stretching vibrations, respectively. NMR was performed to further characterize the molecular structure of DG-CDs. The peaks at 1.31 ppm and 1.53 ppm in the ^{1}H NMR of DG-CDs (Fig. 2j) can be associated with long-chain methylene hydrogens (—CH₂—) in PHMG, especially those located away from the guanidine group. The peaks at 2.7–2.84 ppm were attributed to methylene hydrogens in CA or methylene groups in PHMG close to the guanidine group. The peaks in the range of 3.13–3.86 ppm were attributed to sub methyl (—CH₂—O—) and methyl (—CH—O-) hydrogens from DEX. The ^{13}C NMR (Fig. 2k) showed that the peaks in the range of 39–44 ppm were probably due to the methylene carbon near the guanidinium group, and part of the peaks may be due to the carbon-nitrogen (C—N) bond attached to the guanidinium group. The chemical shifts in the 60–76 ppm region were typically associated with the carbon attached to the oxygen atom of —CH and —CH$_2$ from DEX, particularly the C—OH or C—O—C structures, and the hydroxyl carbon (C—OH) may also occur in this region. In addition, the peaks in the range of 92–96 ppm and 155–157 ppm were typically corresponded to the hemiacetal carbon (C1), and the guanidinium carbon (C═N), respectively. The peaks in the 175–179 ppm were attributed to carboxyl (—COOH) or carboxylic acid ester (C═O) carbons. NMR results imply the inclusion of the molecular structure from the three precursors. The percentage of each element and the chemical composition of DG-CDs were analyzed by XPS. The full-wavelength XPS pattern of DG-CDs showed three main typical peaks (Fig. 2l) of C 1s at 284.8 eV, N 1s at 400.1 eV, and O 1s at 532.4 eV, with the contents of 59.64 %, 11.31 %, and 29.05 %, respectively. The high-resolution C 1s XPS spectra (Fig. 2m) can be fitted to four bands of C—C/C—H (284.3 eV), C—N (285.6 eV), C—O (285.9 eV) and O—C═O (288.4 eV). The high-resolution N 1s XPS spectra (Fig. 2n) exhibited two peaks at 399.6 eV and 400.1 eV. The peak at 399.6 eV represented the nitrogen or common amine in the non-protonated guanidinium group and the peak at 400.1 eV was the nitrogen in the protonated guanidinium group (-NH$_3^+$). The high-resolution O 1s XPS spectra (Fig. 2o) can be fitted to two peaks of O–C═O (530.4 eV) and C—OH/C—O—C (532.0 eV), indicating the presence of carboxyl, hydroxyl, and ether functional groups in the DG-CDs.

Overall, combined with the above characterization and the carbon core structure of CDs [73,74], the carbon nuclei of DG-CDs can be identified as small graphene lamellae or graphene-like structural features (Fig. 3(2)). Furthermore, the surface-active groups of DG-CDs, including C—N/C═N, C—O/C═O, C—O—C, —OH, —COOH, and —NH$_2$, were confirmed by FTIR, NMR, and XPS analysis. Correspondingly, Fig. 3(3) showed the molecular formulae constructed based on the core properties and possible surface functional groups of DG-CDs inferred from the characterization.

3.2. In vitro antibacterial activity of DG-CDs

The MICs of DG-CDs against various bacterial strains were determined for evaluating the antibacterial activity, as shown in Figure S1 and Table S2. DG-CDs demonstrated strong broad-spectrum antibacterial efficacy (Figure S1). For example, the MIC values against MRSA, *S. aureus*, and *S. epidermidis* were 5, 5, and 1.25 μg/mL, respectively. Moreover, the inhibition curves of DG-CDs were investigated. As shown in Fig. 4a and b, the antimicrobial activities of DG-CDs against *S. aureus* and MRSA illustrated a concentration-dependent effect with prolongation of time. When the concentration of DG-CDs was lower than MIC, no significant inhibitory effect was observed after 24 h of exposure. When the concentrations of DG-CDs reached or exceeded its MIC of 5 μg/mL, a significant inhibitory effect was observed. The viabilities of *S. aureus* and MRSA were further assessed by plate counting method. The expected dose-dependent inhibitory activity of DG-CDs on both bacteria were observed (Fig. 4c). Increased DG-CDs caused less survival of *S. aureus* and MRSA, and there were no bacterial colonies after treatment with 10 μg/mL DG-CDs (Fig. 4d and e), confirming the good antibacterial effect of DG-CDs. Related studies have shown that there is a risk of the storage stability of antibacterial nanomaterials [75]. Correspondingly, the stability of the antimicrobial performance of DG-CDs was evaluated in several storage conditions. As shown in Figure S2a, the MIC values of DG-CDs against *S. aureus* and MRSA remained unchanged during long-term storage (360 days). In addition, the DG-CDs still exhibited highly stable antimicrobial activity under a variety of environmental conditions, including treatment with varied temperature from 20 to 90 °C and continuous irradiation with UV lamps (Figure S2b and S2c). Moreover, the antimicrobial efficacies of DG-CDs were unaffected when interfering by 50 % fetal bovine serum, 50 % rabbit serum, trypsin, and proteinase K, respectively (Figure S2d). Considering the practical application of DG-CDs in treating keratitis, the antibacterial stability was evaluated in artificial tear solution and eye drop. As shown in Figure S2e and S2f, DG-CDs maintained stable MIC values throughout the 28-day testing period. These results confirm the storage stability of DG-CDs in a simulated ocular physiological environment (artificial tears) and in an actual medication context (eye drops). These findings indicate that DG-CDs can maintain effective therapeutic activity even when exposed to multiple environments and a prolonged period. The possible progressive development of bacterial resistance of DG-CDs was also evaluated. Using vancomycin as reference control, DG-CDs were successively exposed to sub-inhibitory concentrations of bacterial suspensions. As shown in Fig. 4f and g, the MIC values of DG-CDs against *S. aureus* and MRSA are kept after 30 transmissions, indicating no detectable resistance development. In contrast, vancomycin showed 16-fold higher MIC values against *S. aureus* and MRSA, implying the detectable resistance in the strains. The major advantages of DG-CDs are the stable antibacterial ability with the little potential to induce bacterial resistance.

3.3. Anti-biofilm capability of DG-CDs

Biofilm penetration and eradication of biofilms are challenging due to the protective barrier of EPS. The potentials of DG-CDs to inhibit and eradicate *S. aureus* and MRSA biofilm were investigated. As shown in Fig. 5a and b, DG-CDs inhibited biofilm formation dose-dependently, reducing *S. aureus* and MRSA by 79.9 % and 62.8 % at 40 μg/mL, respectively. The ability of DG-CDs to disrupt the mature biofilm was further investigated. As shown in Fig. 5d and e, after treating by 80 μg/mL DG-CDs, the residual biomass of preformed *S. aureus* and MRSA biofilms were only 31.1 % and 40.6 %, respectively, indicating good ability of removing biofilm. Moreover, bright green fluorescent signals from SYTO9 were observed in the untreated biofilm (Fig. 5g), indicating the complete coverage of live bacteria in the control group. While, the

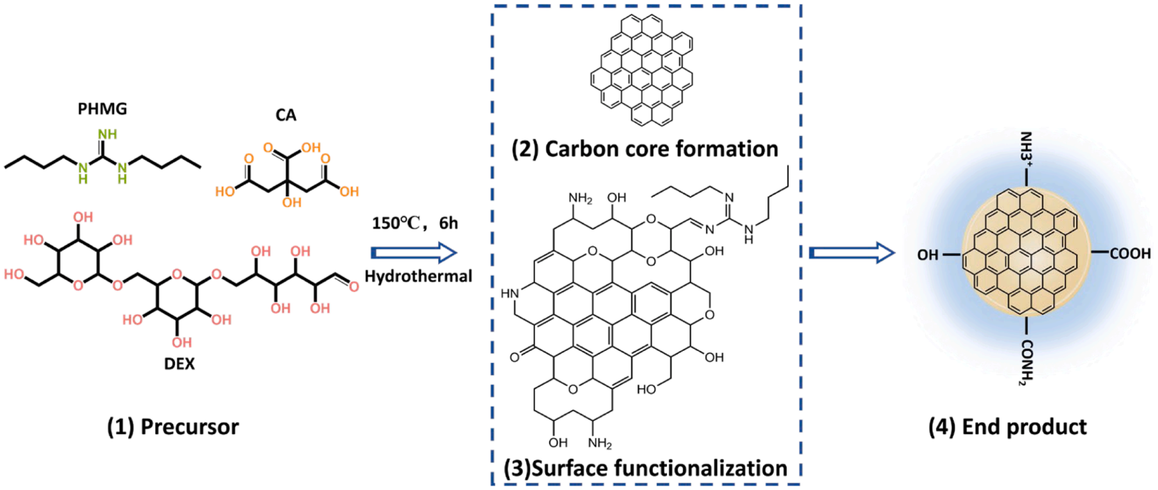

Fig. 3. Simulated molecular structure and final product of DG-CDs based on the synthesis process.

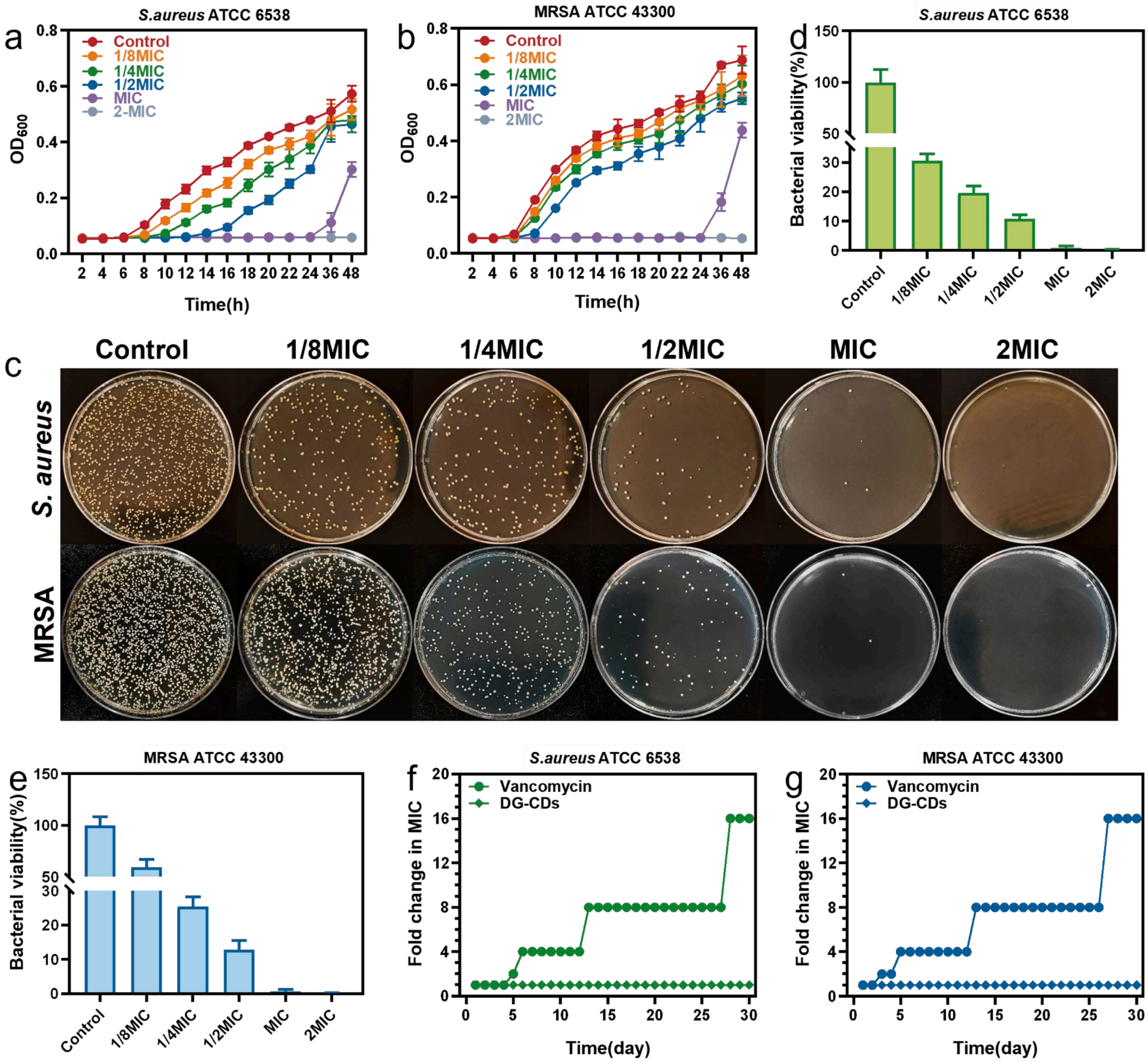

Fig. 4. *In vitro* antibacterial activity evaluation. Inhibition curves of different concentrations of DG-CDs against (a) *S. aureus* and (b) MRSA. (c-e) Results of colony and survival counts of *S. aureus* and MRSA after 24 h co-incubation with different concentrations of DG-CDs. Resistance profile of (f) *S. aureus* and (g) MRSA to DG-CDs and vancomycin.

treated biofilm showed obvious red fluorescent signals from PI with little green field. Moreover, a significant decrease in biofilm thickness and live/dead ratio were also found in the treated biofilms (Fig. 5h), suggesting that DG-CDs can effectively inhibit and eliminate bacterial biofilm. This can be attributed to the fact that the small-sized DG-CDs possess the characteristic groups of dextran, which enhance the penetration and diffusion of DG-CDs into bacterial biofilms through the targeted binding of EPS, accelerating the degradation of the membrane structure for destroy [76,77].

3.4. Evaluating the antibacterial mechanism of DG-CDs

The antibacterial mechanism of DG-CDs was investigated. The morphology of treated bacteria was initially evaluated using SEM (Fig. 6a). *S. aureus* and MRSA were spherical with a complete and intact surface. However, the cell surfaces of treated bacteria appeared hollow and some even ruptured and collapsed with extravasation of cell contents, suggesting that DG-CDs destroy the structural integrity of the bacteria. According to the positive zeta potential of DG-CDs (Fig. 2d), the greatly changed zeta potentials of the incubated bacteria and DG-CDs confirmed that DG-CDs adhered to the negatively charged bacterial surface through electrostatic interactions (Fig. 6b). Unlike eukaryotic cells that use mitochondria to produce energy, bacteria do not have mitochondria. Bacteria heavily rely on ATP as their main energy carrier to drive and regulate complex biochemical processes that are closely linked to energy metabolism within their cells [78]. As shown in Fig. 6c and d, the intracellular ATP of the treated bacteria showed a significant decreased trend with increasing concentrations of DG-CDs. Such findings indicate that DG-CDs can interfere with and even disrupt the normal metabolic mechanism of the bacteria [78], which in turn triggers the reduction of ATP level and ultimately constitutes an inhibitory effect on the survival and reproduction of bacteria.

Bacterial biofilm communities are protected by the EPS matrix [79]. The polysaccharides and proteins in the EPS not only maintain the morphology and structure of the biofilm, but also provide favorable conditions for bacterial attachment, proliferation and protection, sustaining the survival of microorganisms in the biofilm against the penetration of exogenous antimicrobial drugs and thus acquiring high resistance to antimicrobial agents and the host immune system [20]. The effects of DG-CDs on EPS in *S. aureus* and MRSA biofilms were

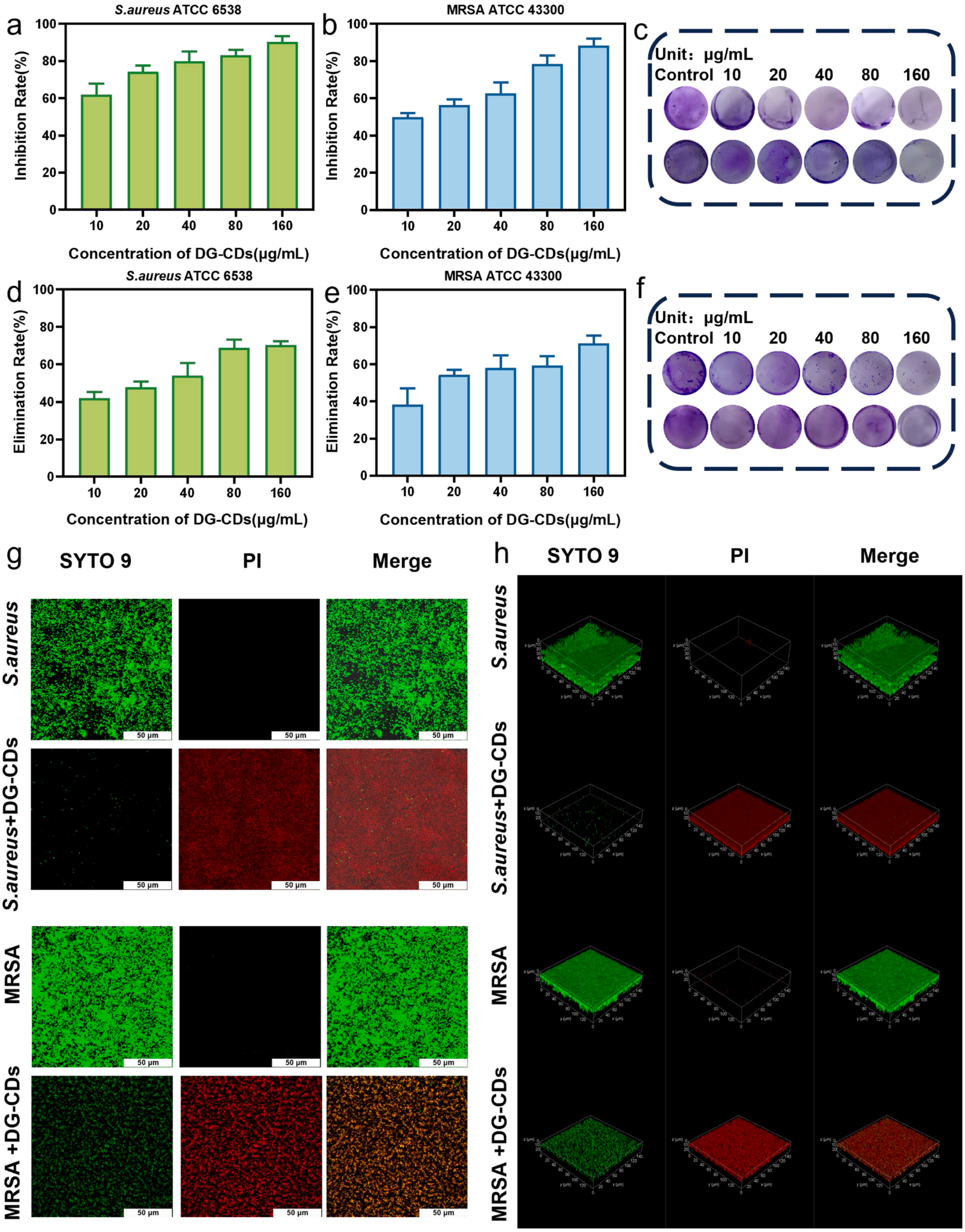

Fig. 5. The evaluation of antibiofilm capacity. Inhibition rate of different concentrations of DG-CDs on biofilm formation of (a) *S. aureus* and (b) MRSA. (c) Crystal violet staining of untreated and different concentrations of DG-CDs inhibiting biofilm formation (*S. aureus* (upper) and MRSA (below)). Clearance rates of different concentrations of DG-CDs on mature biofilms of (d) *S. aureus* and (e) MRSA. (f) Crystal violet staining of mature biofilms damaged by untreated and different concentrations of DG-CDs (*S. aureus* (upper) and MRSA (below)). Live/dead stained CLSM two-dimensional (g) and three-dimensional (h) images of *S. aureus* and MRSA before and after interaction with DG-CDs.

investigated from both polysaccharide and protein aspects (Fig. 6e and f). The contents of polysaccharides and proteins in treated biofilms were reduced to different extents, indicating the differential interactions of DG-CDs with various components of the biofilm. Compared to the control group, the levels of polysaccharides and proteins in *S. aureus* treated with 10 μg/mL DG-CDs were reduced by 68.41 % and 46.7 %, respectively. The relative levels of the corresponding substances in the EPS of MRSA treated with DG-CDs were reduced by 65.3 % and 18.7 %, respectively. These results suggest that the antimicrobial effect of DG-CDs and their inhibition and elimination of biofilms are mainly achieved by disrupting the integrity of the cell membrane and blocking the synthesis and expression of its polysaccharides and extracellular

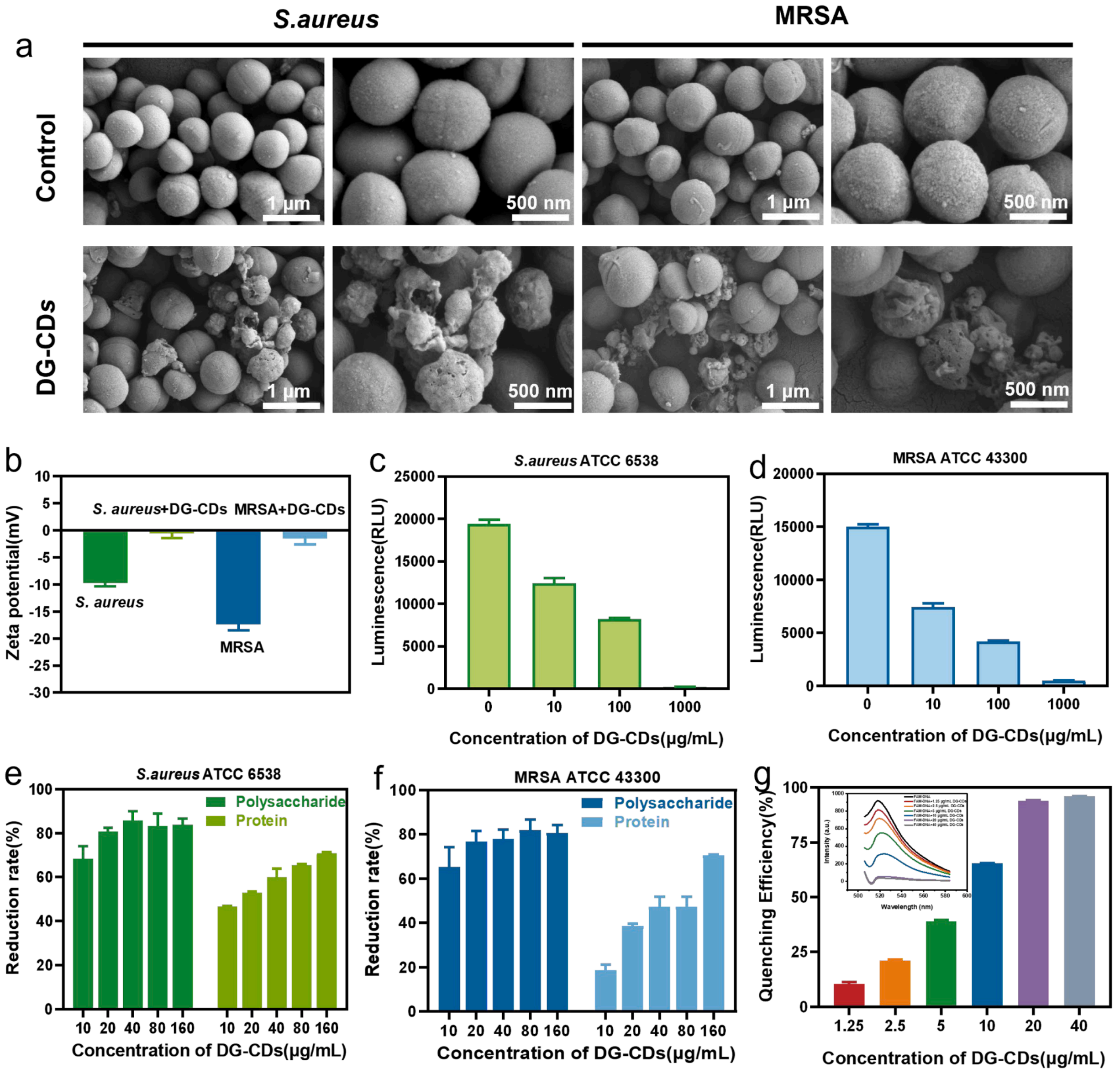

Fig. 6. Antibacterial mechanism of DG-CDs. (a) SEM images of *S. aureus* and MRSA cells before and after treatment with DG-CDs. (b) Zeta potential maps of *S. aureus* and MRSA without and with the interaction of DG-CDs. Changes of intracellular ATP contents of *S. aureus* (c) and MRSA (d) before and after treating by DG-CDs. Changes of polysaccharide and proteins in EPS of *S. aureus* (e) and MRSA (f) after treatment with DG-CDs. (g) Interaction and quenching of FAM labeled DNA on DG-CDs.

proteins.

The interaction between antimicrobials and DNA is directly related to bacterial growth and reproduction [80]. Firstly, the potential interaction between DG-CDs and DNA was simulated and evaluated using FAM labeled ssDNA (FAM-DNA) as probe (Fig. 6g). FAM-DNA had a high fluorescence intensity at 520 nm, while the fluorescence of FAM-DNA was gradually quenched with the addition of increased concentrations of DG-CDs. After the addition of 20 μg/mL DG-CDs, the fluorescence of FAM-DNA was almost completely quenched, indicating that DG-CDs effectively adsorb and interact with DNA, thereby interfering with normal bacterial gene function [81].

Based on membrane breaking results (Fig. 6a), ATP loss (Fig. 6c, d), biofilm inhibition and removal (Fig. 5), and the interacting and interfering foundation of DG-CDs to DNA (Fig. 6g), it was predicted that DG-CDs can interact with several key proteins closely related to bacterial proliferation and virulence. Molecular docking technology, which provides detailed information on ligand-receptor interactions, is a theoretical modelling method for predicting intermolecular binding sites and binding forces [82]. Thus, the molecular docking analysis was carried out to visualize the possible binding models of DG-CDs and specific proteins. In *S. aureus* and MRSA, the cell division protein FtsA plays a pivotal role in bacterial cell division, primarily involved in cell wall synthesis and the formation of the division ring. The ABC transporter ATP-binding protein, a key member of the ABC transporter family, provides energy and regulates the transport of substances across the bacterial membrane. The intercellular adhesion protein R, part of the Ica gene cluster, mediates bacterial adhesion and biofilm formation. The accessory gene regulator protein A, a component of the Agr system, participates in the regulation of bacterial virulence and quorum sensing. DNA primase is a critical enzyme in DNA replication, responsible for initiating the replication process. Penicillin-binding protein mecA is associated with antibiotic resistance in *S. aureus*. Based on the biological functions of these key proteins, FtsA (PDB: 3WQT), ABC-ATPase (PDB: 6XJI), IcaR (PDB: 3GEU), AgrA (PDB: 4G4K), DNA primase (PDB: 4E2K), and PBP2a (PDB: 1VQQ) were selected as targets to analyze their interactions with DG-CDs using molecular docking. The docking results

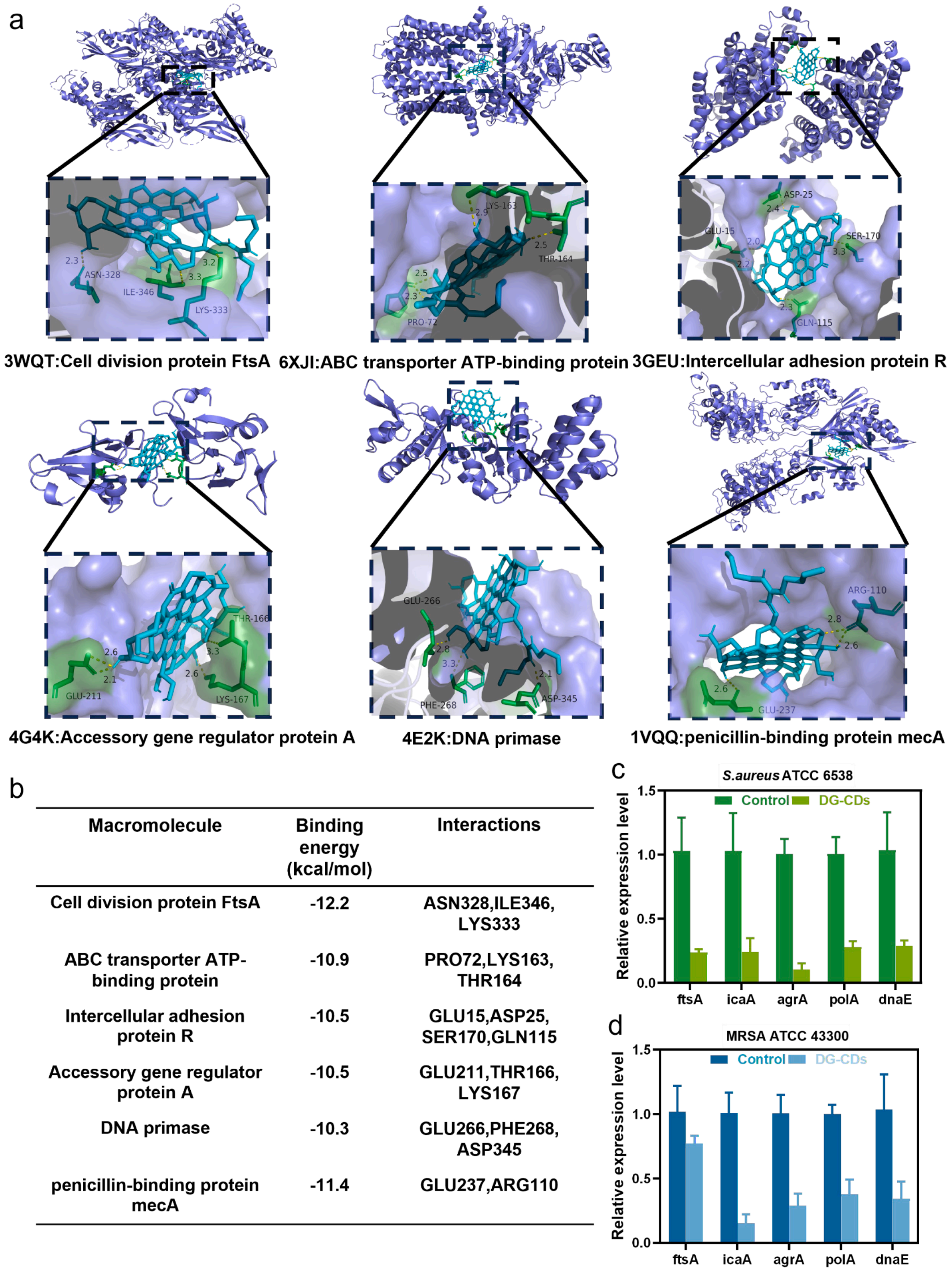

Macromolecule	Binding energy (kcal/mol)	Interactions
Cell division protein FtsA	-12.2	ASN328,ILE346, LYS333
ABC transporter ATP-binding protein	-10.9	PRO72,LYS163, THR164
Intercellular adhesion protein R	-10.5	GLU15,ASP25, SER170,GLN115
Accessory gene regulator protein A	-10.5	GLU211,THR166, LYS167
DNA primase	-10.3	GLU266,PHE268, ASP345
penicillin-binding protein mecA	-11.4	GLU237,ARG110

Fig. 7. Molecular mechanism of the antibacterial ability of DG-CDs. (a) Docking models of DG-CDs with specific proteins. (b) Binding energies and protein–ligand interaction details of DG-CDs with specific proteins by AutoDock Vina. Quantitative analysis of relative expression level of related genes in (c) *S. aureus* and (d) MRSA treated with DG-CDs.

(Fig. 7a, b) indicated that the binding energies of DG-CDs and target proteins were approximately around -10 kcal/mol, suggesting a strong affinity for these targets. Specifically, DG-CDs interfere with the function of FtsA, inhibiting the cell division process and significantly suppressing bacterial proliferation. Binding to ABC-ATPase may affect bacterial transport processes, further limiting bacterial growth and resistance. DG-CDs bind to IcaR, potentially impairing bacterial adhesion and biofilm formation. Through interactions with AgrA, DG-CDs regulate the expression of genes involved in virulence factors and biofilm formation, thereby attenuating bacterial pathogenicity. DG-CDs also interfere with DNA replication by binding to DNA primase, further inhibiting bacterial growth. Finally, DG-CDs may inhibit the function of the antibiotic resistance protein PBP2a, reducing bacterial resistance to antibiotics. In conclusion, the significant binding of DG-CDs to multiple critical targets highlights their potential to inhibit bacterial proliferation, virulence, adhesion, biofilm formation, and antibiotic resistance. This molecular-level analysis provides theoretical support for the antimicrobial mechanisms of DG-CDs and offers valuable insights for optimizing the structure of CDs as antimicrobials.

Following the results of the above experiments and molecular docking, RT-qPCR was used to examine the expression levels of relevant genes in *S. aureus* and MRSA (Fig. 7c, d). The FtsA protein, encoded by the ftsA gene, is essential for cell division of bacteria. The expression of the ftsA gene was downregulated 4.19-fold in S. aureus and 1.29-fold in MRSA treated by DG-CDs. In addition, polA and dnaE genes, which encode DNA polymerases, are responsible for chromosome replication. The genes of polA and dnaE were significantly downregulated in both *S. aureus* and MRSA after treatment with DG-CDs. These results indicate that DG-CDs have significant effects in interfering bacterial division and DNA replication.

Polysaccharide intercellular adhesin (PIA), a key factor in biofilm formation, is synthesized under the regulation of the icaA gene, which is negatively regulated by icaR. The balance between icaA and icaR plays a critical role in controlling biofilm production. AgrA, encoded by the agrA gene, regulates biofilm formation and quorum sensing (QS), influencing antibiotic resistance. As shown in Fig. 7c and d, the expressions of icaA and agrA were downregulated 4.13-fold and 9.36-fold in S. aureus, and 6.51-fold and 3.43-fold in MRSA after DG-CDs treatment, respectively. These results suggest that DG-CDs effectively inhibit biofilm formation and disrupt AgrA-mediated signaling in the QS system.

Considering the broad-spectrum antimicrobial activity of DG-CDs and the severity of bacterial resistance, MRSA was selected as the model bacterium to carry out the transcriptome sequencing assay to further reveal the above clarified antibacterial mechanism of DG-CDs at the molecular level. Volcano plot analysis (Figure S3a) identified a total of 1151 differentially expressed genes (DEGs), including 549 significantly upregulated and 602 significantly downregulated genes. To further illustrate representative expression changes, a hierarchical clustering heatmap of several key DEGs was generated (Figure S3b), highlighting distinct expression patterns between the DG-CDs-treated and control groups. GO classification at level 2 (Figure S3c) and KEGG enrichment analysis of the top 20 pathways (Figure S3d), both based on identified DEGs, comprehensively revealed the major biological functions and signaling pathways involved. Further GO and KEGG enrichment analyses suggest that the antimicrobial activity of DG-CDs is closely associated with multiple essential biological processes and regulatory pathways (Figure S4a, S4b).

Specifically, DG-CDs interfere with cell division by downregulating key genes related to cell division (GO:0051301) and the cell cycle (GO:0007049), such as ftsA and ftsZ, thereby disrupting the normal formation of the division ring and inhibiting bacterial proliferation. Additionally, the impairment of the peptidoglycan biosynthesis (ko00550) pathway weakens the stability of the cell wall, leading to damage to membrane integrity (GO:0071840) and causing leakage of cellular contents, ultimately significantly reducing bacterial survival. DG-CDs significantly downregulate genes involved in DNA repair (GO:0006281), nucleic acid metabolism (GO:0090304), and cellular responses to DNA damage (GO:0006974), affecting pathways such as mismatch repair (ko03430), base excision repair (ko03410), and nucleotide excision repair (ko03420), thereby compromising genomic stability. Transcriptomic analysis further reveals the downregulation of polA and dnaE, key genes in DNA replication and repair, consistent with PCR results. DG-CDs significantly downregulate metabolic pathways such as carbon metabolism (ko01200), the pentose phosphate pathway (ko00030), and one-carbon metabolism (ko00670), weakening bacterial energy supply and metabolic capacity. Moreover, disruption of aminoacyl-tRNA biosynthesis (ko00970) impairs protein translation efficiency, broadly weakening bacterial physiological functions. DG-CDs regulate processes involved in cell component organization (GO:0051128), significantly impairing key processes related to biofilm matrix synthesis and intercellular adhesion. The downregulation of specific elements, such as the agr system and the spa gene, indicates that DG-CDs disrupt bacterial quorum sensing systems, weakening cell aggregation and hindering biofilm initiation and maturation. A downregulation of icaR expression was found in transcriptomic analysis. As mentioned above, icaR acts as a negative regulator by binding to the icaR operon and inhibiting the expression of icaA and other genes related to biofilm formation. This result seems to contradict the conclusion from RT-qPCR, where icaA expression was found to be downregulated. It is speculated that DG-CDs indirectly influence the expression of icaR and icaA by regulating their common upstream targets [83-85]. Further omics analysis indicates the upregulation of the fur gene and the downregulation of the luxR gene. Both fur and luxR also play important roles in the formation and regulation of bacterial biofilms. Fur primarily regulates iron homeostasis and the expression of related virulence genes, thereby influencing bacterial growth, pathogenicity, and biofilm formation [86,87]. As a negative regulator, fur typically suppresses the expression of genes associated with biofilm formation, particularly by inhibiting the expression of the ica operon. Therefore, the upregulation of fur may indirectly affect the formation and stability of bacterial biofilms. On the other hand, luxR is a key transcriptional regulator in quorum sensing systems. In various bacterial species, luxR activates or represses downstream genes related to biofilm formation, virulence, and motility by recognizing and binding to autoinducer molecules [88–90]. The downregulation of luxR expression suggests that the presence of DG-CDs may interfere with the quorum sensing pathways, thereby impairing the regulatory mechanisms of biofilm formation and reducing both pathogenicity and biofilm structural integrity. DG-CDs significantly downregulate core genes related to vancomycin resistance (ko01502), such as pbp2a, thus weakening MRSA's resistance to glycopeptide antibiotics and enhancing the synergistic bactericidal effect of antibiotics. Finally, the protein-protein interaction (PPI) network of differentially expressed genes (DEGs) constructed based on the STRING database further reveals the interactions among these genes (Figure S5). These results align closely with the *in vitro* antibacterial experiments and offer crucial molecular evidence for the antimicrobial mechanism of DG-CDs, affirming their ability to disrupt bacterial physiological activities at multiple levels.

Based on *in vitro* antibacterial experiments, molecular docking results, RT-qPCR, and omics, the antimicrobial mechanism of DG-CDs involves a multi-step process leading to bacterial damage. DG-CDs adsorb onto the bacterial surface, enter the cells, and interact with key intracellular targets, such as DNA and proteins. This interference disrupts bacterial function with several significant physiological changes, including structural damage, ATP leakage, and ultimate rupture and apoptosis.

3.5. Immunomodulatory capacity of DG-CDs

The immune system plays a significant role in the pathogenesis and repair process of keratitis. The potential immunoregulatory properties of DG-CDs were assessed. As shown in Fig. 8a, under non-inflammatory conditions, DG-CDs at different concentrations promoted macrophage polarization toward the M1 phenotype. Additionally, the proportion of M2 macrophages gradually increased with increased DG-CDs (Fig. 8a and b). When the concentration reached 80 μg/mL, the proportion of M1 macrophages was approximately 39.4 %, while the proportion of M2 macrophages was approximately 7.9 %. These results suggest that, in the absence of inflammation or during the early stages of infection, DG-CDs promote the conversion of macrophages toward the M1 phenotype, thereby enhancing inflammation, bacterial clearance, and the recruitment of early immune cells. However, under simulated infectious inflammatory conditions (Fig. 8c and d), low concentrations of DG-CDs still exhibited a modest promoting effect on M1 polarization. When the concentration of DG-CDs reached 80 μg/mL, the proportion of M1 macrophages decreased, whereas the proportion of M2 macrophages increased, resulting in a reduced M1/M2 ratio (Figure S6c), with approximately 50.4 % of cells being in the M2 state or transitioning toward the M2 phenotype (Fig. 8d). These findings suggest that, under

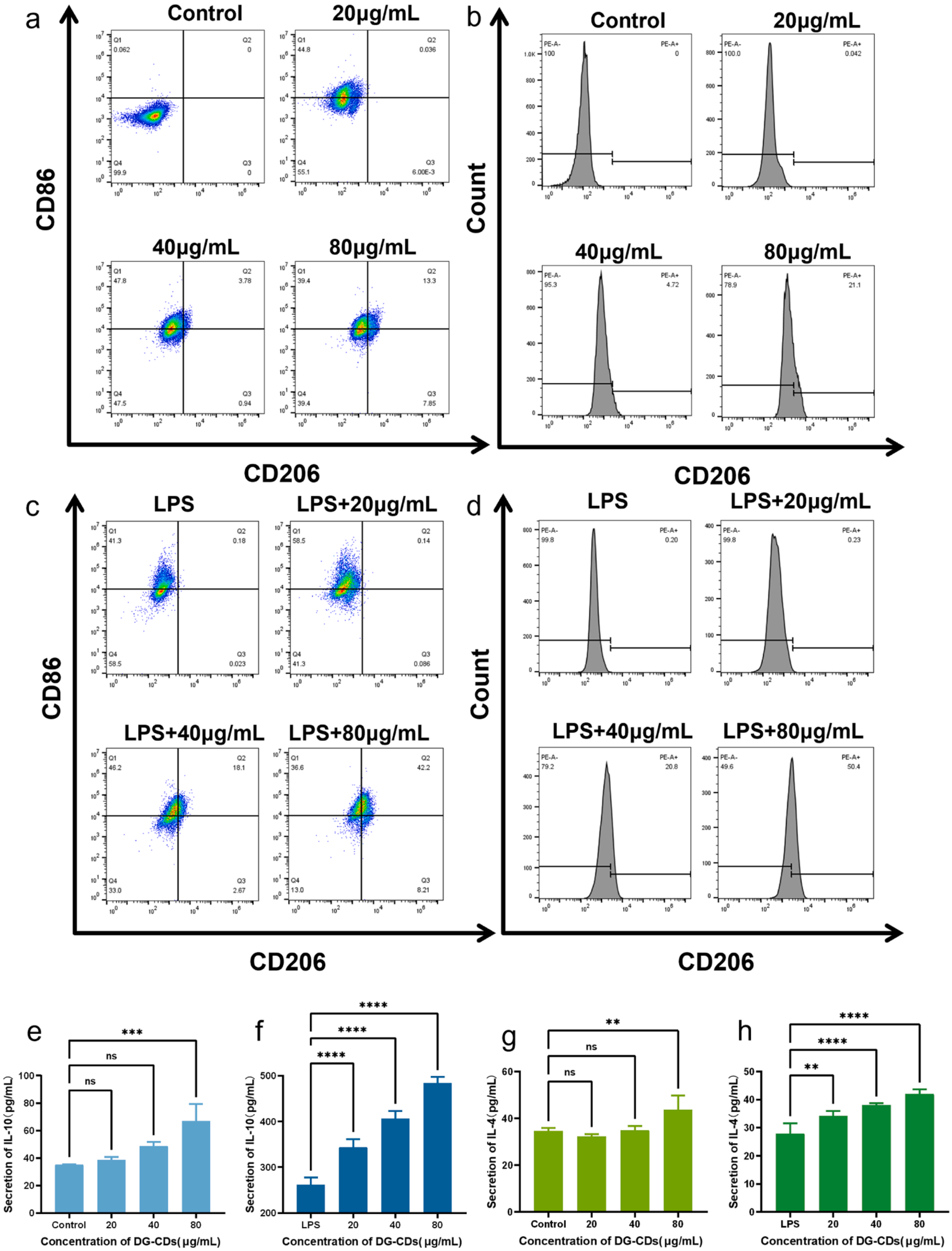

Fig. 8. Immunomodulatory capacities of DG-CDs. The effect of DG-CDs on M1 and M2 polarization (a, c) of macrophages under normal (a) and inflammatory (c) conditions. The effect of DG-CDs on M2 polarization (b, d) of macrophages under normal (b) and inflammatory (d) conditions. Change in IL-10 (e, f) and IL-4 (g, h) concentrations in macrophage supernatant under non-inflammatory (e, g) and inflammatory (f, h) conditions.

inflammatory conditions, DG-CDs at 80 μg/mL facilitate the polarization of M1 macrophages toward the M2 phenotype, thus promoting inflammation regulation and tissue repair. IL-4 and IL-10 are closely associated with the polarization and secretion of M2 macrophages. Correspondingly, IL-4 and IL-10 were selected to further validate the immune-regulatory effects of DG-CDs. As shown in Fig. 8e and f, IL-10 gradually increased with the elevation of DG-CDs concentration under both untreated macrophage and LPS-treated macrophage, consistent with the flow cytometry results of promoting macrophage M2 polarization. When the DG-CDs concentration reached 80 μg/mL, the IL-10 concentration increased to more than twice that of the control group. Although IL-4 exhibited a similar trend to IL-10, its concentration was significantly lower (Fig. 8g and h). This may be because IL-4 is primarily secreted by T cells and mast cells in smaller amounts [91].

3.6. Evaluation of the safety and in vivo treating effect of DG-CDs

The cytocompatibility and hemocompatibility of DG-CDs were investigated. The effects of different concentrations of DG-CDs on HK-2 (human normal kidney cells) and HLE-B3 (human lens epithelial cells) were assessed using CCK-8 assay kits. Fig. 9a and b showed the cell viabilities of HK-2 cells and HLE-B3 cells after co-culturing with different concentrations of DG-CDs for 24 h. Compared with the control group, DG-CDs exhibited little impact on the viabilities of HK-2 cells or HLE-B3 cells. Even at a 40-fold MIC concentration, the 200 μg/mL DG-CDs demonstrated good cytocompatibility, with the cell viability levels of 77.38 % and 78.43 %, respectively. This favorable biocompatibility can be attributed to the low affinity of DG-CDs to mammalian cells [92]. Furthermore, as shown in Fig. 9c, the positive group was red due to the release of hemoglobin, whereas the supernatant of DG-CDs was as clear as that of the negative group. The hemolysis rate was significantly lower than 5 % when introducing 320 μg/mL DG-CDs, suggesting the good hemocompatibility of DG-CDs. In addition, before formally establishing the MRSA-infected rat keratitis model (Fig. 9d and e), saline, vancomycin and DG-CDs were administered to the eyes of normal rats by a simulated eye drop method, and the ocular irritation of all three groups were assessed by slit lamp microscopy within 24 h. Fig. 9e showed that there was no significant ocular abnormality between the saline group and the administered group. Sodium fluorescein staining under cobalt blue light showed a clear and intact cornea, suggesting the little damage of DG-CDs. The mean ocular irritation score in the vancomycin and DG-CDs groups was lower than 3 (Table S3), which was not significantly different from the saline group's score. These results confirm that DG-CDs have good *in vitro* and *in vivo* biosafety.

A model of MRSA-infected rat keratitis was established to evaluate the *in vivo* therapeutic effect of DG-CDs as eye drops (Fig. 9d). The post-infected rat eyes were examined by slit lamp under diffuse light and cobalt blue light (Fig. 9e). After 3 days of treatment in the saline group, the cornea remained cloudy and edematous, and the iris texture and

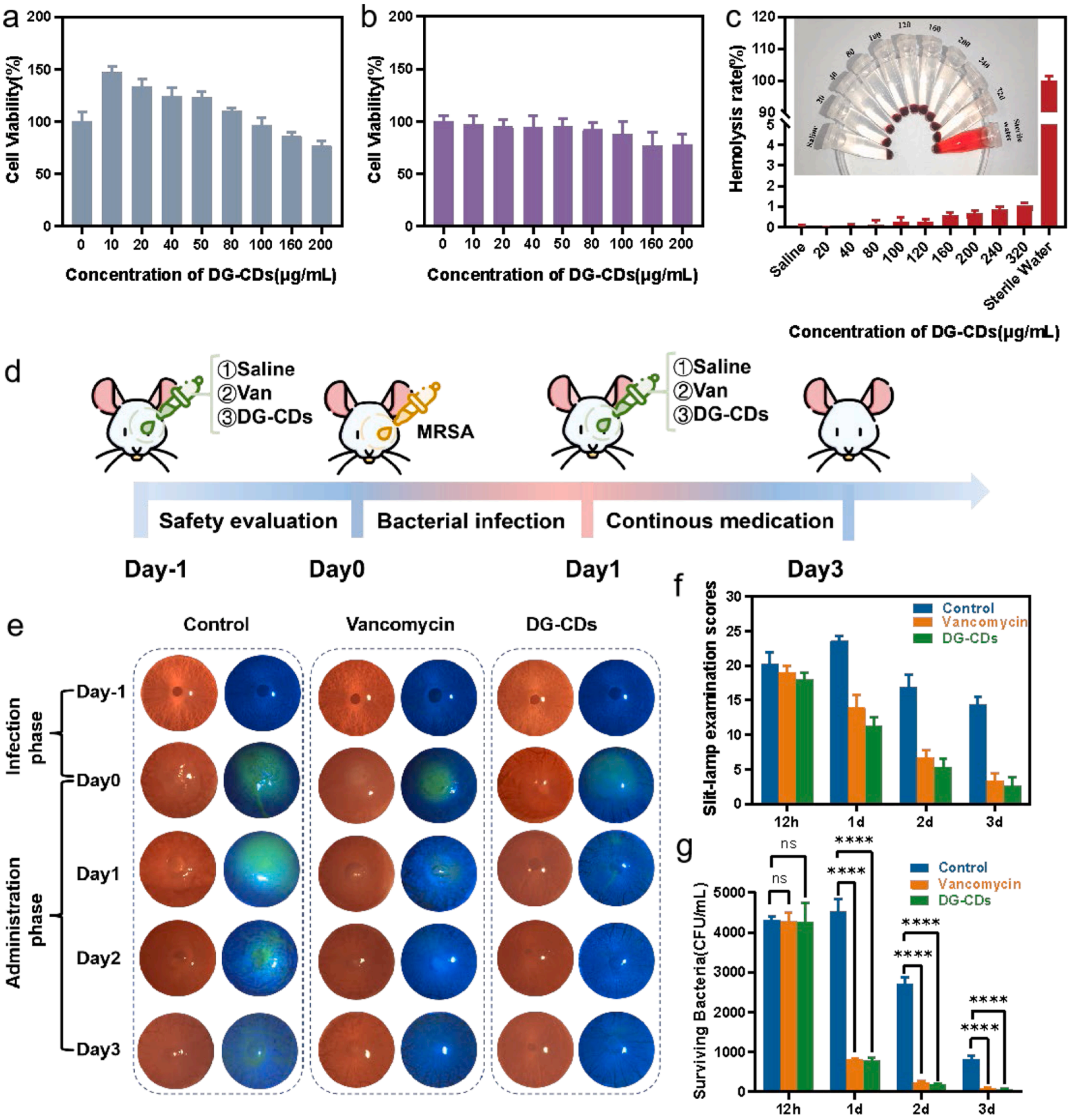

Fig. 9. Biosafety and *in vivo* application of DG-CDs. cell viability of HK-2 cells (a) and HLE-B3 cells (b) after 24 h of co-culture with different concentrations of DG-CDs. (c) Hemocompatibility of DG-CDs. (d) Scheme of the construction of MRSA-infected rat keratitis model. (e) Diffuse and cobalt blue light examination of the eyes of infected and treated rats by slit lamp. (f) Quantitative evaluation of clinical scores (g) Bacterial survival of rat corneas within 1–3 days of treatment. (For interpretation of the references to color in this figure legend, the reader is referred to the web version of this article.).

pupil contour were not recognizable. In contrast, the vancomycin and DG-CDs effectively suppressed MRSA infection throughout the entire treatment process. Although there was still a small amount of incomplete repair and slight edema in the corneal epithelial layer, the corneas in the vancomycin and DG-CDs groups were significantly clearer than those in the saline group. The treatment effect was further assessed quantitatively using the clinical scores (Fig. 9f). These results indicate that DG-CDs exhibit strong anti-infective activity and good therapeutic effect on BK. To further verify the inhibitory and clearing effects of DG-CDs on MRSA in BK models, agar plate colonies in daily corneal tissues were coated (Figure S7) and quantitatively studied (Fig. 9g).The number of MRSA colonies in all three groups gradually decreased with the prolongation of the treatment time (Fig. 9g), indicating that the eye itself has a certain self-cleaning function. The bacterial counts in the vancomycin and DG-CDs groups were significantly lower than those in the saline group, suggesting that vancomycin and DG-CDs can substantially inhibit the ocular bacterial growth thereby controlling the infection in the first instance of the bacterial transmission. Notably, DG-CDs were more effective than vancomycin in terms of shorter disease duration and reduction in colony size (Fig. 9e-g and S7).

The histological analysis was carried out. Compared with the illustration and thickness of the normal cornea (Figure S8), H&E staining showed that the corneal interstitial tissue layer was significantly edematous in the saline group (Fig. 10a), and the thickness of the corneal interstitial layer was 406.43 μm, which was greater than that of the normal cornea (Fig. 10b). Under infectious stimulation, a large infiltration of immune cells, such as neutrophils, occurred in the corneal stroma, while inflammatory cytokines promoted tissue edema and stromal cell activation, leading to fluid accumulation and loosening of the stromal structure. Additionally, the direct damage caused by bacterial toxins and metabolites further exacerbated these changes, resulting in significant thickening of the corneal tissue observed in H&E staining (Fig. 10a). The vancomycin and DG-CDs groups showed epithelial and stromal thicknesses comparable to normal corneas, indicating the effects of both vancomycin and DG-CDs in alleviating infectious corneal structural damage. Therefore, the saline group exhibited more inflammatory cells and extensive inflammatory cell infiltration through H&E staining. The vancomycin group restored normal corneal thickness but still retained certain inflammatory cells, whereas the DG-CDs group showed significantly fewer inflammatory cells (Fig. 10a). This is because although vancomycin may indirectly reduce the overreaction of the immune system by removing the source of infection, the toxins (*e.g.* endotoxin) released after bacterial death may continue to stimulate the immune system, resulting in a persistent inflammatory

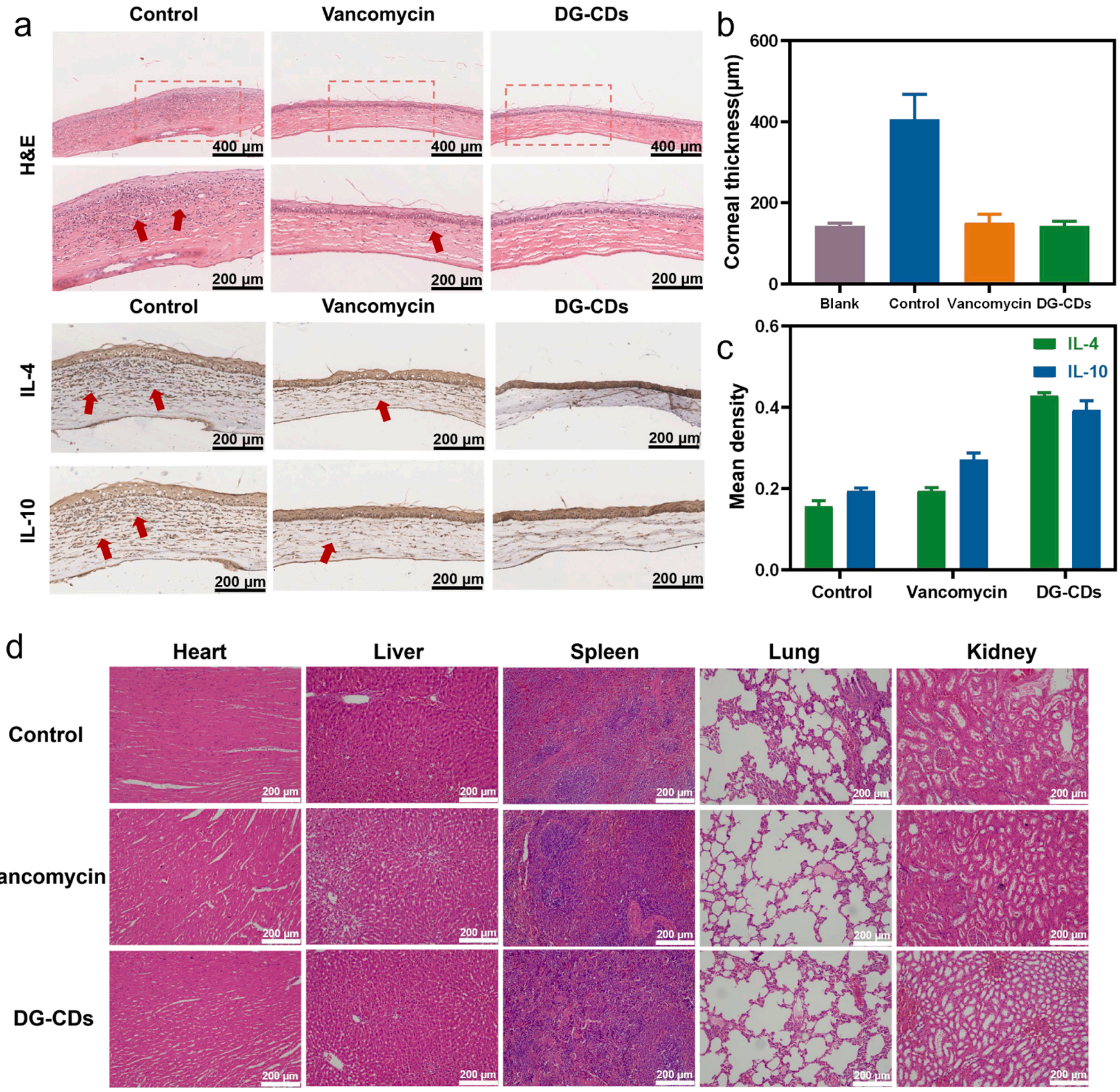

Fig. 10. Pathological analysis of the *in vivo* BK models. (a) Corneal H&E staining and immunohistochemical results. (b) Quantitative results of corneal interstitial layer thickness. (c) Quantitative results of inflammatory factor expression levels. (d) H&E staining results of heart, liver, spleen, lung, and kidney tissues in rats.

response. Vancomycin, on the other hand, does not actively regulate the function of the immune system and does not directly address the immune overreaction or the inflammatory response itself. At this point, antibiotics alone may not fully resolve the issue, as immune system overreaction can still cause tissue damage of corneal stroma degradation, opacity, fibrosis, and nerve damage [93]. These effects are primarily driven by proteases and reactive oxygen species released by neutrophils, leading to further disruption of corneal transparency and structural integrity, potentially resulting in permanent vision impairment [94]. Therefore, in clinical practice, a combination of immunomodulatory drugs is often required to achieve optimal therapeutic outcomes [95]. The dual function of DG-CDs can act as an antibacterial agent to rapidly control inflammation and inhibit immune overreaction.

The expression levels of inflammatory factors in the cornea were further investigated using immunohistochemical analysis (Fig. 10a). The results showed that the saline group had significantly increased corneal thickness with extensive inflammatory cell infiltration, indicating a strong inflammatory response. The vancomycin group exhibited corneal thickness close to normal but still showed some inflammatory cells, suggesting partial relief of inflammation without complete resolution. The DG-CDs group displayed near-normal corneal thickness with significantly fewer inflammatory cells, demonstrating effective inflammation reduction. These findings are consistent with H&E staining, further confirming the differences in therapeutic effects and inflammation regulation among the groups. The quantitative analysis of IL-4 and IL-10 in the corneal tissues (Fig. 10c) illustrated that the levels of IL-4 and IL-10 in the DG-CDs group were significantly higher than those in the saline and vancomycin groups, and proved that DG-CDs had a better therapeutic effect of reducing inflammation and promoting trauma repair. Furthermore, H&E staining of the heart, liver, spleen, lungs, and kidneys from the rats of different groups (Fig. 10d) implied that no histological differences or toxic reactions were observed after treatment with DG-CDs.

4. Conclusion

In this work, DG-CDs with dual functions broad-spectrum antibacterial activity and immunomodulatory properties were synthesized. Besides the antibacterial activity, we elucidated the underlying mechanisms by demonstrating that DG-CDs disrupted key genes involved bacterial cell division, quorum sensing, biofilm formation, and DNA replication and repair. Moreover, the DG-CDs exhibited biocompatibility with normal cells and tissues. *In vivo* experiments illustrated that DG-CDs not only significantly inhibited the growth of bacteria on the corneal surface, but also promoted inflammation resolution and subsequent corneal healing in rat BK models by MRSA. Histopathological analyses further confirmed that DG-CDs provided enhanced healing effects compared to conventional antibiotics, which was attributed to their antibacterial and immunomodulatory capabilities. DG-CDs are expected to become a strong competitor to traditional contact lens care solutions or eye drops, not only because they can effectively prevent microbial contamination that may occur during contact lens use, but also because they can be applied directly to the eye as a safe and highly effective treatment for bacterial keratitis.

CRediT authorship contribution statement

Menghan Zhang: Writing – original draft, Methodology, Investigation, Formal analysis, Data curation, Conceptualization. **Yiyang Wang:** Writing – original draft, Methodology, Investigation, Formal analysis, Data curation. **Chenfang Miao:** Methodology, Investigation, Formal analysis. **Shuwei Lin:** Investigation, Data curation. **Ying Zheng:** Methodology, Investigation. **Xiaoyan Lin:** Data curation. **Yao Wang:** Methodology, Investigation. **Xinhua Lin:** Resources. **Xiaofeng Zhu:** Supervision. **Shaohuang Weng:** Writing – review & editing, Writing – original draft, Supervision, Project administration, Funding acquisition, Conceptualization.

Declaration of competing interest

The authors declare that they have no known competing financial interests or personal relationships that could have appeared to influence the work reported in this paper.

Acknowledgements

The authors thank Prof. Yan Huang from the School of Medical Technology and Engineering, Fujian Medical University for the discussion of the *in vivo* experiment. The authors thank Prof. Yancheng Wen from the Department of Pathogenic Biology, Fujian Medical University for the discussion of the discussion of the bacterial mechanisms. The authors thank Mr. Zhihong Huang from the Public Technology Service Center Fujian Medical University for the operation of CLSM in this work. This work is financially supported from the Joint Funds for the Innovation of Science and Technology, Fujian Province (2021Y9007), and the Fujian Provincial Financial Health Provincial Special Subsidy Funds (BPB-2023ZXF). Shuwei Lin thank the College Students' Innovation and Entrepreneurship Training Program (JC2023059).

Supplementary materials

Supplementary material associated with this article can be found, in the online version, at doi:10.1016/j.actbio.2025.05.032.

References

[1] D.H. Dang, K.M. Riaz, D. Karamichos, Treatment of non-infectious corneal injury: review of diagnostic agents, therapeutic medications, and future targets, Drugs 82 (2) (2022) 145–167.
[2] R.R. Mohan, D. Kempuraj, S. D'Souza, A. Ghosh, Corneal stromal repair and regeneration, Prog. Retin. Eye Res. 91 (2022) 101090.
[3] M. Cabrera-Aguas, P. Khoo, S.L. Watson, Infectious keratitis: a review, Clin. Exp. Ophthalmol. 50 (5) (2022) 543–562.
[4] L. Ung, J. Chodosh, Foundational concepts in the biology of bacterial keratitis, Exp. Eye Res. 209 (2021) 108647.
[5] S. Tuft, T.F. Somerville, J.O. Li, T. Neal, S. De, M.J. Horsburgh, J.L. Fothergill, D. Foulkes, S. Kaye, Bacterial keratitis: identifying the areas of clinical uncertainty, Prog. Retin. Eye Res. 89 (2022) 101031.
[6] R.B. Singh, S. Das, J. Chodosh, N. Sharma, M.E. Zegans, R.P. Kowalski, V. Jhanji, Paradox of complex diversity: challenges in the diagnosis and management of bacterial keratitis, Prog. Retin. Eye Res. 88 (2022) 101028.
[7] L. Ung, J. Chodosh, Urgent unmet needs in the care of bacterial keratitis: an evidence-based synthesis, Ocul. Surf. 28 (2023) 378–400.
[8] H.I. Ahmad, A. Jabbar, N. Mushtaq, Z. Javed, M.U. Hayyat, J. Bashir, I. Naseeb, Z. U. Abideen, N. Ahmad, J. Chen, Immune tolerance *vs.* Immune resistance: the interaction between host and pathogens in infectious diseases, Front. Vet. Sci. 9 (2022) 827407.
[9] A.J. Wolf, D.M. Underhill, Peptidoglycan recognition by the innate immune system, Nat. Rev. Immunol. 18 (4) (2018) 243–254.
[10] J. Liu, Z. Li, Resident innate immune cells in the cornea, Front. Immunol. 12 (2021) 620284.
[11] M.J. Sweet, D. Ramnath, A. Singhal, R. Kapetanovic, Inducible antibacterial responses in macrophages, Nat. Rev. Immunol. 25 (2025) 92–107.
[12] S.D. Kobayashi, F.R. DeLeo, M.T. Quinn, Microbes and the fate of neutrophils, Immunol. Rev. 314 (1) (2023) 210–228.
[13] K.H. Rasmussen, C.L. Hawkins, Role of macrophage extracellular traps in innate immunity and inflammatory disease, Biochem. Soc. Trans. 50 (1) (2022) 21–32.
[14] T.W. Carion, M. Greenwood, A.S. Ebrahim, A. Jerome, S. Suvas, K. Gronert, E. A. Berger, Immunoregulatory role of 15-lipoxygenase in the pathogenesis of bacterial keratitis, FASEB J. 32 (9) (2018) 5026–5038.
[15] R.J. O'Callaghan, The pathogenesis of Staphylococcus aureus eye infections, Pathogens 7 (1) (2018).
[16] A. Austin, T. Lietman, J. Rose-Nussbaumer, Update on the management of infectious keratitis, Ophthalmology 124 (11) (2017) 1678–1689.
[17] J.G. Pearce, R.W. Essex, T. Maddess, The clinical treatment of bacterial keratitis: a review of drop instillation regimes, Cont. Lens. Anterior. Eye 45 (6) (2022) 101725.
[18] L. Urwin, K. Okurowska, G. Crowther, S. Roy, P. Garg, E. Karunakaran, S. MacNeil, L.J. Partridge, L.R. Green, P.N. Monk, Corneal infection models: tools to investigate the role of biofilms in bacterial keratitis, Cells 9 (11) (2020) 2450.
[19] A. Lin, M.K. Rhee, E.K. Akpek, G. Amescua, M. Farid, F.J. Garcia-Ferrer, D.M. Varu, D.C. Musch, S.P. Dunn, F.S. Mah, Bacterial keratitis preferred practice pattern®, Ophthalmology 126 (1) (2019) p1-p55.

[20] X. Li, D. Chen, S. Xie, Current progress and prospects of organic nanoparticles against bacterial biofilm, Adv. Colloid. Interface Sci. 294 (2021) 102475.
[21] A. Abbas, A. Barkhouse, D. Hackenberger, G.D. Wright, Antibiotic resistance: a key microbial survival mechanism that threatens public health, Cell Host. Microbe 32 (6) (2024) 837–851.
[22] I. Nakajima, K. Fukuda, W. Ishida, T. Kishimoto, A. Kuwana, T. Suzuki, C. Kaito, K. Yamashiro, Staphylococcus aureus-derived virulent phenol-soluble modulin α triggers alarmin release to drive IL-36-dependent corneal inflammation, Microbes. Infect. 26 (1–2) (2024) 105237.
[23] K. Fukuda, W. Ishida, A. Fukushima, T. Nishida, Corneal fibroblasts as sentinel cells and local immune modulators in infectious keratitis, Int. J. Mol. Sci. 18 (9) (2017) 1831.
[24] Y. Peng, S. Pang, Y. Zeng, J. Wei, J. Lu, Y. Ruan, X. Hong, X. He, X. Chu, Y. Guo, H. Guo, S. Qian, Z. Jiang, Z. Jiang, B. Wang, Antibiotic-free ocular sterilization while suppressing immune response to protect corneal transparency in infectious keratitis treatment, J. Control Release 374 (2024) 563–576.
[25] S.Y. Kim, J.E. Lee, Resolvin D1 inhibits corneal inflammation in Staphylococcus Aureus Keratitis, Ocul. Immunol. Inflamm. 31 (5) (2023) 927–934.
[26] G. Sosne, E.A. Berger, Thymosin beta 4: a potential novel adjunct treatment for bacterial keratitis, Int. Immunopharmacol. 118 (2023) 109953.
[27] L.D. Hazlett, X. Jiang, S.A. McClellan, IL-10 function, regulation, and in bacterial keratitis, J. Ocul. Pharmacol. Ther. 30 (5) (2014) 373–380.
[28] L. Guibo, D. Chunxu, C. Biao, H. Zhaolei, L. Wenwen, J. Xiangnan, P. Wentao, C. Hongmin, L. Yonghua, Z. Guoqiang, Dectin-1 participates in the immune-inflammatory response to mouse Aspergillus fumigatus keratitis by modulating macrophage polarization, Front. Immunol. 15 (2024) 1431633.
[29] S.A. Mohid, P. Sharma, A. Alghalayini, T. Saini, D. Datta, M.D.P. Willcox, H. Ali, S. Raha, A. Singha, D. Lee, N. Sahoo, C.G. Cranfield, S. Roy, A. Bhunia, A rationally designed synthetic antimicrobial peptide against Pseudomonas-associated corneal keratitis: structure-function correlation, Biophys. Chem. 286 (2022) 106802.
[30] R. Rosini, S. Nicchi, M. Pizza, R. Rappuoli, Vaccines against antimicrobial resistance, Front. Immunol. 11 (2020) 1048.
[31] Q. Xin, H. Shah, A. Nawaz, W. Xie, M.Z. Akram, A. Batool, L. Tian, S.U. Jan, R. Boddula, B. Guo, Q. Liu, J.R. Gong, Antibacterial carbon-based nanomaterials, Adv. Mater. 31 (45) (2019) e1804838.
[32] Y. Wang, Y. Yang, Y. Shi, H. Song, C. Yu, Antibiotic-free antibacterial strategies enabled by nanomaterials: progress and perspectives, Adv. Mater. 32 (18) (2020) e1904106.
[33] Y. Zhang, A. Li, Y. Zhang, S. Hong, Y. Xue, X. Song, J. Li, S. Huang, X. Zhang, Bacteria-targeting nanosilver-based antibacterial drugs for efficient treatment of drug-resistant bacterial-infected keratitis, Macromol. Rapid. Commun. 44 (23) (2023) e2300379.
[34] J. Xiang, R. Zou, P. Wang, X. Wang, X. He, F. Liu, C. Xu, A. Wu, Nitroreductase-responsive nanoparticles for *in situ* fluorescence imaging and synergistic antibacterial therapy of bacterial keratitis, Biomaterials 308 (2024) 122565.
[35] S.A. Khan, S. Shahid, T. Mahmood, C.S. Lee, Contact lenses coated with hybrid multifunctional ternary nanocoatings (Phytomolecule-coated ZnO nanoparticles: Gallic Acid: tobramycin) for the treatment of bacterial and fungal keratitis, Acta Biomater. 128 (2021) 262–276.
[36] Y. Fang, L. Zhuo, H. Yuan, H. Zhao, L. Zhang, Construction of graphene quantum dot-based dissolving microneedle patches for the treatment of bacterial keratitis, Int. J. Pharm. 639 (2023) 122945.
[37] S. Ch, M. Paul, S.G. Padaga, B. Ghosh, S. Biswas, Cationized gelatin-sodium alginate polyelectrolyte nanoparticles encapsulating moxifloxacin as an eye drop to treat bacterial keratitis, Int. J. Biol. Macromol. 264 (Pt 1) (2024) 130457.
[38] S. Liu, Q. Bai, Y. Jiang, Y. Gao, Z. Chen, L. Shang, S. Zhang, L. Yu, D. Yang, N. Sui, Z. Zhu, Multienzyme-like nanozyme encapsulated ocular microneedles for keratitis treatment, Small. 20 (21) (2024) e2308403.
[39] H. Han, Y. Gao, M. Chai, X. Zhang, S. Liu, Y. Huang, Q. Jin, A. Grzybowski, J. Ji, K. Yao, Biofilm microenvironment activated supramolecular nanoparticles for enhanced photodynamic therapy of bacterial keratitis, J. Control Release 327 (2020) 676–687.
[40] C. Yu, Y. Gao, Y. Zhang, J. Wang, Y. Zhang, J. Li, X. Zhang, Z. Wu, X. Zhang, A targeted photosensitizer mediated by visible light for efficient therapy of bacterial keratitis, Biomacromolecules 22 (9) (2021) 3704–3717.
[41] J. Zhang, H. Dong, B. Liu, D. Yang, Biomimetic materials for antibacterial applications, Small 21 (2025) 2408543.
[42] Y. Bai, L. Ma, Y. Huang, S. Lang, W. Fan, G. Liu, Zwitterionic silver nanoparticle based antibacterial eye drops for efficient therapy of bacterial keratitis, Biomater. Sci. 11 (22) (2023) 7397–7407.
[43] A.C.M. de Paiva, M.D.C. Ferreira, A.S. da Fonseca, Photodynamic therapy for treatment of bacterial keratitis, Photodiagnosis. Photodyn. Ther. 37 (2022) 102717.
[44] Y. Bai, Y. Hu, Y. Gao, X. Wei, J. Li, Y. Zhang, Z. Wu, X. Zhang, Oxygen self-supplying nanotherapeutic for mitigation of tissue hypoxia and enhanced photodynamic therapy of bacterial keratitis, ACS Appl. Mater. Interfaces. 13 (29) (2021) 33790–33801.
[45] M. Ran, R. Sun, J. Yan, A.T. Pulliainen, Y. Zhang, H. Zhang, DNA nanoflower eye drops with antibiotic-resistant gene regulation ability for MRSA keratitis target treatment, Small. 19 (47) (2023) e2304194.
[46] Y.B. Chen, X.F. Wan, Y. Yue, S. He, J. Cao, W.X. He, T.T. Tai, D. Wang, Z.K. Zhou, Y. Deng, Low-intensity ultrasound-activated cavitation effect triggers piezoelectric catalysis coordinating Respiratory chain interference tactics against bacterial infection, Adv. Funct. Mater. 22 (2024) 2419426.
[47] X. Guan, Z. Li, X. Geng, Z. Lei, A. Karakoti, T. Wu, P. Kumar, J. Yi, A. Vinu, Emerging trends of carbon-based quantum dots: nanoarchitectonics and applications, Small 19 (17) (2023) e2207181.
[48] B.Y. Wang, H.Q. Song, X.L. Qu, J.B. Chang, B. Yang, S.Y. Lu, Carbon dots as a new class of nanomedicines: opportunities and challenges, Coord. Chem. Rev. 442 (2021) 18.
[49] Y. Wu, C. Li, H.C. van der Mei, H.J. Busscher, Y. Ren, Carbon quantum dots derived from different Carbon sources for antibacterial applications, Antibiotics 10 (6) (2021) 623.
[50] Y. Hu, O. Seivert, Y. Tang, H.E. Karahan, A. Bianco, Carbon dot synthesis and purification: trends, challenges and recommendations, Angew. Chem. Int. Ed. 63 (48) (2024) e202412341.
[51] D. Zhao, M. Xu, K. Dai, H. Liu, Y. Jiao, X. Xiao, The preparation of chiral carbon dots and the study on their antibacterial abilities, Mater. Chem. Phys. 295 (2023) 127144.
[52] V.B. Kumar, Z. Porat, A. Gedanken, Synthesis of doped/hybrid carbon dots and their biomedical application, Nanomaterials 12 (6) (2022) 898.
[53] E. Sviridova, A. Barras, A. Addad, E. Plotnikov, A. Di Martino, D. Deresmes, K. Nikiforova, M. Trusova, S. Szunerits, O. Guselnikova, P. Postnikov, R. Boukherroub, Surface modification of carbon dots with tetraalkylammonium moieties for fine tuning their antibacterial activity, Biomater. Adv. 134 (2022) 112697.
[54] A. Verma, F. Arshad, K. Ahmad, U. Goswami, S.K. Samanta, A.K. Sahoo, M.P. Sk, Role of surface charge in enhancing antibacterial activity of fluorescent carbon dots, Nanotechnology. 31 (9) (2020) 095101.
[55] S. Huang, Y. Song, J.R. Zhang, X. Chen, J.J. Zhu, Antibacterial carbon dots-based composites, Small. 19 (31) (2023) e2207385.
[56] W.B. Zhao, K.K. Liu, Y. Wang, F.K. Li, R. Guo, S.Y. Song, C.X. Shan, Antibacterial carbon dots: mechanisms, design, and applications, Adv. Healthc. Mater. 12 (23) (2023) e2300324.
[57] M. Yu, P. Li, R. Huang, C. Xu, S. Zhang, Y. Wang, X. Gong, X. Xing, Antibacterial and antibiofilm mechanisms of carbon dots: a review, J. Mater. Chem. B 11 (4) (2023) 734–754.
[58] K.J. Mintz, M. Bartoli, M. Rovere, Y.Q. Zhou, S.D. Hettiarachchi, S. Paudyal, J. Y. Chen, J.B. Domena, P.Y. Liyanage, R. Sampson, D. Khadka, R.R. Pandey, S. X. Huang, C.C. Chusuei, A. Tagliaferro, R.M. Leblanc, A deep investigation into the structure of carbon dots, Carbon 173 (2021) 433–447.
[59] B. Yao, H. Huang, Y. Liu, Z. Kang, Carbon dots: a small conundrum, Trends. Chem. 1 (2) (2019) 235–246.
[60] A.R. Nallayagari, E. Sgreccia, R. Pizzoferrato, M. Cabibbo, S. Kaciulis, E. Bolli, L. Pasquini, P. Knauth, M.L. Di Vona, Tuneable properties of carbon quantum dots by different synthetic methods, J. Nanostructure Chem. 12 (4) (2022) 565–580.
[61] X. Deng, M. Zhang, Y. Wang, C. Li, X. Zhang, S. Weng, Y. Li, Carbon dots with selective fluorescence response to hydroxyl radical for sensitive detection of bleomycin, Spectrochim. Acta A 306 (2024) 123582.
[62] X. Deng, M. Zhang, Y. Wang, C. Miao, Y. Zheng, J. Huang, Y. Chen, S. Weng, A facile fluorescence method for the effective detection of ampicillin using antioxidant carbon dots with specific fluorescent response to •OH, Analyst 149 (13) (2024) 3651–3660.
[63] P. Paul, R. Nair, S. Mahajan, U. Gupta, M. Aalhate, I. Maji, P.K. Singh, Traversing the diverse avenues of exopolysaccharides-based nanocarriers in the management of cancer, Carbohydr. Polym. 312 (2023) 120821.
[64] Z. Liu, K. Guo, L. Yan, K. Zhang, Y. Wang, X. Ding, N. Zhao, F.J. Xu, Janus nanoparticles targeting extracellular polymeric substance achieve flexible elimination of drug-resistant biofilms, Nat. Commun. 14 (1) (2023) 5132.
[65] M. Li, X. Lan, X. Han, S. Shi, H. Sun, Y. Kang, J. Dan, J. Sun, W. Zhang, J. Wang, Acid-induced self-catalyzing platform based on dextran-coated copper peroxide nanoaggregates for biofilm treatment, ACS Appl. Mater. Interfaces. 13 (25) (2021) 29269–29280.
[66] L. Dordevic, F. Arcudi, M. Cacioppo, M. Prato, A multifunctional chemical toolbox to engineer carbon dots for biomedical and energy applications, Nat. Nanotechnol. 17 (2) (2022) 112–130.
[67] P. Pham, S. Oliver, E.H.H. Wong, C. Boyer, Effect of hydrophilic groups on the bioactivity of antimicrobial polymers, Polym. Chem. 12 (39) (2021) 5689–5703.
[68] L. Yu, Y. Wang, K. Li, X. Li, M. He, C. Chen, F. Li, B. Liang, L. Li, N. Gu, Z. Liu, B. Li, G. Wang, J. Fan, Metformin-based carbon dots based on biguanide functional groups for simultaneous chelation of copper ions and inhibitable colorectal cancer therapy, Carbon 212 (2023) 118095.
[69] S. Hui, Carbon dots (CDs): basics, recent potential biomedical applications, challenges, and future perspectives, J. NanoPart Res. 25 (4) (2023) 44.
[70] D.W. Boukhvalov, V.Y. Osipov, D. Murzalinov, A. Serikkanov, H. Bi, A comprehensive model of carbon nanodots with 0.21 nm lattice fringes patterns, Carbon 225 (2024) 119101.
[71] J.B. Wu, M.L. Lin, X. Cong, H.N. Liu, P.H. Tan, Raman spectroscopy of graphene-based materials and its applications in related devices, Chem. Soc. Rev. 47 (5) (2018) 1822–1873.
[72] V. Mochalin, S. Osswald, Y. Gogotsi, Contribution of functional groups to the Raman spectrum of nanodiamond powders, Chem. Mater. 21 (2) (2009) 273–279.
[73] A.T. Krasley, E. Li, J.M. Galeana, C. Bulumulla, A.G. Beyene, G.S. Demirer, Carbon nanomaterial fluorescent probes and their biological applications, Chem. Rev. 124 (6) (2024) 3085–3185.
[74] M.K. Barman, A. Patra, Current status and prospects on chemical structure driven photoluminescence behaviour of carbon dots, J Photochem Photobiol C 37 (2018) 1–22.

[75] W. Huang, F. Tao, F. Li, M. Mortimer, L.-H. Guo, Antibacterial nanomaterials for environmental and consumer product applications, NanoImpact. 20 (2020) 100268.

[76] P.C. Naha, Y. Liu, G. Hwang, Y. Huang, S. Gubara, V. Jonnakuti, A. Simon-Soro, D. Kim, L. Gao, H. Koo, D.P. Cormode, Dextran-coated iron oxide nanoparticles as biomimetic catalysts for localized and pH-activated biofilm disruption, ACS Nano 13 (5) (2019) 4960–4971.

[77] J. Li, K. Zhang, L. Ruan, S.F. Chin, N. Wickramasinghe, H. Liu, V. Ravikumar, J. Ren, H. Duan, L. Yang, M.B. Chan-Park, Block copolymer nanoparticles remove biofilms of drug-resistant gram-positive bacteria by nanoscale bacterial debridement, Nano Lett. 18 (7) (2018) 4180–4187.

[78] R. Mackieh, N. Al-Bakkar, M. Kfoury, R. Roufayel, J.M. Sabatier, Z. Fajloun, Inhibitors of ATP synthase as new antibacterial candidates, Antibiotics 12 (4) (2023) 650.

[79] L. Dieltjens, K. Appermans, M. Lissens, B. Lories, W. Kim, E.V. Van der Eycken, K. R. Foster, H.P. Steenackers, Inhibiting bacterial cooperation is an evolutionarily robust anti-biofilm strategy, Nat. Commun. 11 (1) (2020) 107.

[80] H.J. Jian, R.S. Wu, T.Y. Lin, Y.J. Li, H.J. Lin, S.G. Harroun, J.Y. Lai, C.C. Huang, Super-cationic carbon quantum dots synthesized from spermidine as an eye drop formulation for topical treatment of bacterial keratitis, ACS Nano 11 (7) (2017) 6703–6716.

[81] M.A. Jhonsi, D.A. Ananth, G. Nambirajan, T. Sivasudha, R. Yamini, S. Bera, A. Kathiravan, Antimicrobial activity, cytotoxicity and DNA binding studies of carbon dots, Spectrochim. Acta A. 196 (2018) 295–302.

[82] C. Zhong, L. Ke, F. Hu, Z. Lin, S. Ye, Z. Zheng, S. Han, Z. Lin, Y. Zhan, Y. Hu, P. Shi, L. Wen, H. Yao, Ginsenoside Rb1 inhibits cardiomyocyte apoptosis and rescues ischemic myocardium by targeting caspase-3, J. Pharm. Anal. (2024), https://doi.org/10.1016/j.jpha.2024.101142.

[83] Q. Peng, X. Tang, W. Dong, N. Sun, W. Yuan, A review of biofilm formation of Staphylococcus aureus and its regulation mechanism, Antibiotics 12 (1) (2022) 12.

[84] S. Gao, Y. Wang, S. Yuan, J. Zuo, W. Jin, Y. Shen, D. Grenier, L. Yi, Y. Wang, Cooperation of quorum sensing and central carbon metabolism in the pathogenesis of gram-positive bacteria, Microbiol. Res. 282 (2024) 127655.

[85] D. Mack, P. Becker, I. Chatterjee, S. Dobinsky, J.K. Knobloch, G. Peters, H. Rohde, M. Herrmann, Mechanisms of biofilm formation in Staphylococcus epidermidis and Staphylococcus aureus: functional molecules, regulatory circuits, and adaptive responses, Int. J. Med. Microbiol. 294 (2–3) (2004) 203–212.

[86] J. Rom, D. Atwood, K. Beenken, D. Meeker, A. Loughran, H. Spencer, T. Lantz, M. Smeltzer, Impact of Staphylococcus aureus regulatory mutations that modulate biofilm formation in the USA300 strain LAC on virulence in a murine bacteremia model, Virulence 8 (8) (2017) 1776–1790.

[87] Q. Yu, H. Li, L. Du, L. Shen, J. Zhang, L. Yuan, H. Yao, H. Xiao, Q. Bai, Y. Jia, J. Qiu, Y. Li, Transcriptional regulation of the yersiniabactin receptor fyuA gene by the ferric uptake regulator in Klebsiella pneumoniae NTUH-K2044, J. Basic Microbiol. 64 (8) (2024) e2400001.

[88] R. Chaparian, M. Tran, L. Miller Conrad, D. Rusch, J. van Kessel, Global H-NS counter-silencing by LuxR activates quorum sensing gene expression, Nucleic. Acids. Res. 48 (1) (2020) 171–183.

[89] U. Paswan, H. Basak, S. Saha, A. Chatterjee, In silico screening of FDA-approved anthelmintic drugs against LuxR protein as quorum-sensing inhibitors and exploration of their binding mechanism and electronics properties, ChemistrySelect. 9 (40) (2024) e202402317.

[90] F. Maggio, C. Rossi, A. Serio, C. Chaves-Lopez, M. Casaccia, A. Paparella, Anti-biofilm mechanisms of action of essential oils by targeting genes involved in quorum sensing, motility, adhesion, and virulence: a review, Int. J. Food Microbiol. 426 (2024) 110874.

[91] A. Kelly-Welch, E.M. Hanson, A.D. Keegan, Interleukin-4 (IL-4) pathway, Sci. STKe 2005 (293) (2005) cm9.

[92] X. Hao, L. Huang, C. Zhao, S. Chen, W. Lin, Y. Lin, L. Zhang, A. Sun, C. Miao, X. Lin, M. Chen, S. Weng, Antibacterial activity of positively charged carbon quantum dots without detectable resistance for wound healing with mixed bacteria infection, Mater. Sci. Eng. C 123 (2021) 111971.

[93] M.A. Stepp, A.S. Menko, Immune responses to injury and their links to eye disease, Transl. Res. 236 (2021) 52–71.

[94] N. Fortingo, S. Melnyk, S.H. Sutton, M.A. Watsky, W.B. Bollag, Innate immune system activation, inflammation and corneal wound healing, Int. J. Mol. Sci. 23 (23) (2022) 14933.

[95] S. Medhasi, A. Chindamporn, N. Worasilchai, A. Review, Antimicrobial therapy for human pythiosis, Antibiotics 11 (4) (2022) 450.